How criticality meets bifurcation in compressive failure of disordered solids

Ashwij Mayya, Estelle Berthier, Laurent Ponson

How criticality meets bifurcation in compressive failure of disordered solids

Ashwij Mayya, Estelle Berthier,* and Laurent Ponson†
Institut Jean Le Rond D'Alembert UMR 7190, Sorbonne Université, CNRS, Paris, France
(Dated: June 28, 2022)

Continuum mechanics describes compressive failure as a standard bifurcation in the response of a material to an increasing load: damage, which initially grows uniformly in the material, localizes within a thin band at failure. Yet, experiments recording the acoustic activity preceding localization evidence power-law distributed failure precursors of increasing size, suggesting that compressive failure is a critical phenomenon. We examine here this apparent contradiction by probing the spatial organization of the damage activity and its evolution until localization during compression experiments of 2D cellular solids. The intermittent damage evolution measured in our experiments is adequately described by a non-stationary depinning equation derived from damage mechanics and reminiscent of critical phenomena. In this description, precursors are damage cascades emerging from the interplay between the material's disorder and the long-range stress redistributions following individual damage events. Yet, the divergence of their characteristic size close to failure, which we observe in our experiments, is not the signature of a transition towards criticality. Instead, the system remains at a fixed distance to the critical point at all stages of the damage evolution. The divergence results from the progressive loss of stability of the material as it is driven towards localization. Thus, our study shows that compressive failure is a standard bifurcation for which the material disorder plays a marginal role. It also shows that precursory activity constitute by-products of the evolution towards localization and can serve to build a predictive method to assess the residual lifetime of structures.

Damage localization is the standard mode of failure of materials under compression. Decoding this degradation process is therefore the cornerstone of the design of reliable and safe structures such as buildings, bridges, tunnels and a countless number of mechanical parts under compressive loading conditions. During their life in service, these structures may progressively lose their mechanical integrity. Comprehending damage evolution to predict their remaining lifetime is an essential component of modern tools of structural design and predictive maintenance. Yet, the appropriate theoretical concepts for describing damage spreading and ultimately localization are still vigorously debated and constitute an active topic of research [1–4].

Continuum damage mechanics is a powerful approach for describing the compressive failure of materials such as rocks, ceramics or mortar [5–8]. In this framework, discrete damage mechanisms like microcrack growth are described at a continuum scale through the degradation of the local elastic stiffness of the material [9–13]. Beyond some critical load level, this softening leads to a bifurcation from the homogeneous damage field to a localized damage that only grows within a thin band and leading to material failure [14, 15].

In parallel, and almost independently to the development of damage mechanics, the intermittent dynamics of damage growth preceding compressive failure has attracted a lot of attention. Acoustic emissions have been used as a preferential means of experimental investigation. Experimental measurements reveal that damage grows through bursts that display robust scale-free statistics [6, 10, 16–24]. Accounting for material disorder, various theoretical works [25–29] have proposed to describe failure as a discontinuous (first-order) phase transition where the precursory damage events emerge from the sweeping of an instability. These ideas are primarily discussed in the context of toy models of failure, using e.g. random fuse models. As a result, a direct comparison with the statistical properties of precursors measured experimentally is not possible, leaving unresolved the applicability of these concepts to real materials. Motivated by the observation of an increase of the precursors' size close to localization [21, 24, 30–33], an alternative scenario in which compressive failure is described as a continuous (second-order) phase transition was also proposed [24, 31, 34–39]: similarly to a large range of driven disordered elastic systems [40–42], the bursts of activity characterizing the response of damaging materials are interpreted as critical fluctuations, or avalanches, that are reminiscent of the so-called depinning transition, a critical phenomenon emerging from the competition between disorder and elastic interactions. Above a depinning threshold, damage is thus expected to grow at some finite speed, eventually leading to failure. When approaching this critical point, the material should then display scale-free fluctuations with diverging length and time scales, a feature that has been observed in some compression experiments [24, 39].

Despite the appeal of such a scenario, it comes in direct contradiction with continuum damage models which describe compressive failure as a standard bifurcation in the equivalent homogeneous material response, for which material disorder and hence precursors play a minor role. To uncover the role of precursors and their connection with compressive failure, one seeks to reconcile these two seemingly incompatible approaches. Recently, we exam-

ined this issue in a 1D toy model [43]. However, the generalization of our results to real materials was limited by the short-range interactions and the system dimension considered in our model. Here, we follow a different approach: we start from the in-depth characterization of the damage precursors in a model experimental system to subsequently confront our observations with these two competing scenarios.

EXPERIMENTAL INVESTIGATION OF FAILURE PRECURSORS

Damage localization

Taking inspiration from Poirier *et al.*'s experiments [44], we perform compression tests of 2D hexagonal packings of soft cellular solids (Fig. 1*A*). Damage spreading in the bi-dimensional specimen at the scale of the individual cells is tracked in space and time using a high speed camera. We thus circumvent the drawbacks inherent to X-ray tomography that provides the detailed spatial structure of damage events in 3D materials but at the cost of temporal resolution [45, 46]. We also overcome the limitations of acoustic emissions that provide highly resolved time series but with a rather poor spatial resolution [47, 48]. First, we focus on the average mechanical response of the specimen. A typical force-displacement curve recorded during a compression test under displacement control conditions (see Materials and Methods) is shown in Fig. 1*B*. As evidenced from the snapshots of the experiments taken at different load levels (top inset of Fig. 1*B* and Supplementary Video S1), the specimen initially deforms rather uniformly, even beyond the linear elastic regime. Considering the deviation to cell circularity as a measure of damage level, damage grows homogeneously from the elastic limit $F = F_{\rm el}$ until the peak load $F = F_{\rm c}$ (refer to Table. S1 for a list of notations), except for the cells close to the boundary where friction is dominant. However, after peak load, a band consisting of progressively collapsing cells appears, initiating from the top corners of the structure. The localization band is clearly visible further away from peak load, as shown on the snapshot in the upper right corner of Fig. 1*B*. The onset loading $\Delta_{\rm c}$ of localization is inferred from the evolution of the vertical strain $\langle\epsilon_{\rm yy}\rangle_{\mathcal{R}_2}$ averaged over the bottom region $\mathcal{R}_2$ of the specimen (indicated on Fig. 1A): as displayed in the lower inset of Fig. 1*B*, for $\Delta > \Delta_{\rm c}$, $\langle\epsilon_{\rm yy}\rangle_{\mathcal{R}_2}$ saturates and departs from the strain $\epsilon_{\rm yy}^{\rm ext}$ imposed by the loading machine. On the contrary, the strain $\langle\epsilon_{\rm yy}\rangle_{\mathcal{R}_1}$ measured in the upper region $\mathcal{R}_1$ follows the imposed strain. This confirms that damage localization starts at peak load.

This behavior is perfectly consistent with continuum damage mechanics that predicts the emergence of the localization band at peak load [14, 15, 49] (see SI Sec. S3F for the analytical prediction). If the experiments were under force control conditions, as in most real-life structural applications, a sudden collapse of the cells resulting in the catastrophic failure of the specimen would also occur at peak load.

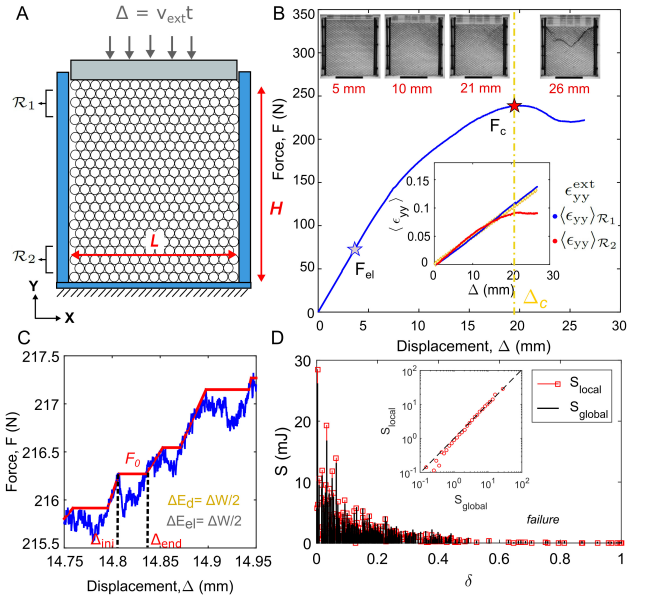

FIG. 1. (A) Schematic of the compression experiment depicting the front view of the hexagonal packing of soft cellular solids. Owing to the displacement Δ applied to the specimen through a piston moving at a rate $v_{\rm ext}$, the cells undergo a deformation that is recorded using a high speed camera. (B) Typical force-displacement response of the specimen. Top insets: The emergence of a localization band of collapsed cells, corresponding to highly localized deformations, is visible on the snapshots of the specimen taken at different load levels. Bottom inset : The strain level averaged over the bottom region $\mathcal{R}_2$ indicated in panel (A) saturates after localization for $\Delta > \Delta_{\rm c}$ while the one measured in the upper region $\mathcal{R}_1$ follows the linear trend $\epsilon_{\rm yy}^{\rm ext} = \Delta/H = v_{\rm ext}\, t/L$ imposed by the loading machine. (C) Construction of an equivalent force control experiment from the mechanical response of the specimen measured under displacement control. The start and the end of a damage precursor taking place at a constant force F_0 are denoted by $\Delta_{\rm ini}$ and $\Delta_{\rm end}$. The precursor size $S_{\rm global} = \Delta E_{\rm d}$ defined as the dissipated energy during the event corresponds to half the work of the external force $\Delta W = F_0\,(\Delta_{\rm end} - \Delta_{\rm ini})$. (D) Variations of the precursor size S, in terms of dissipated energy, with the distance to failure δ. Inset : Comparison of precursor sizes computed from the global analysis and the local analysis.

Precursors as cascades of damage events

We now analyze the precursory damage activity taking place before peak load. A closer examination of the force-displacement curve in Fig. 1*C* reveals sudden force drops of amplitude much larger than the precision ± 0.05 N of our load cell. These drops are followed by a linear in-

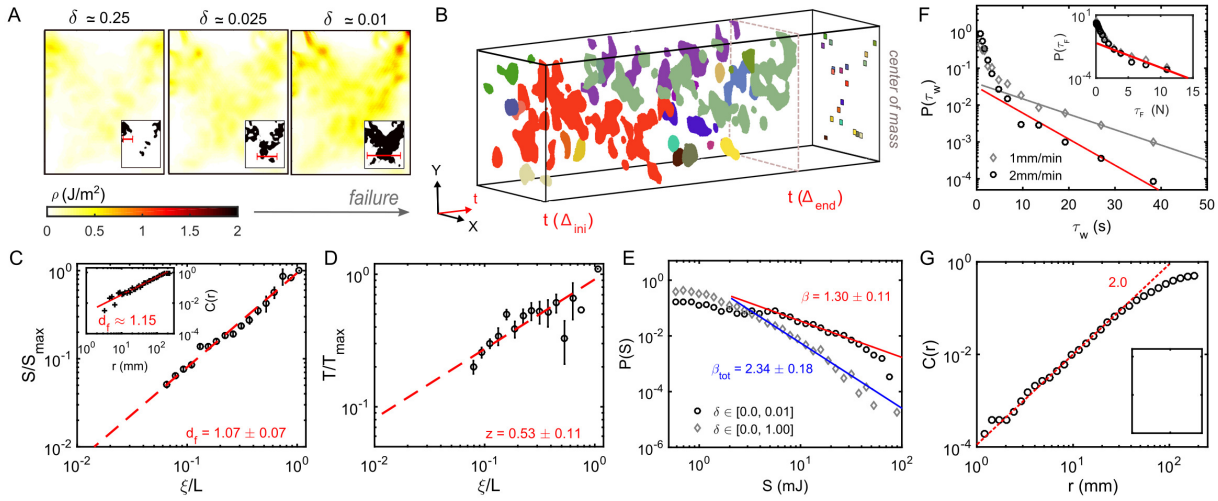

FIG. 2. (A) Energy density maps, $\rho(\vec{x})$, and their corresponding binary thresholded formats (inset) of energy dissipation at various distances to failure in a typical experiment. The spatial extent of the cascades extracted using the auto-correlation of the thresholded maps are denoted by the red bracket in the inset. (B) Evolution of clusters within a cascade (second panel in (A), at $\delta \simeq 0.025$), the center of mass of each cluster is shown in the background. Here, the third axis is time and each cluster is indicated by a given color. The largest clusters appear in multiple slices of time. Scaling of the size (in terms of dissipated energy) (C) and duration (D) of cascades, normalized by their maximum values, as a function of their characteristic spatial extent ξ, normalized by the system size L. Inset in (C) : Pair correlation function of the centers of mass of the clusters within a cascade permitting to extract the fractal dimension $d_f \simeq 1.15$. (E) Distribution of the cascade sizes obtained during the whole duration of experiments (diamonds) and in the vicinity of final failure (circles). (F) Distribution of waiting time between cascades. The waiting time is defined as the difference in time-stamps of the arrival of two successive avalanches $\tau_w(\mathrm{s}) = t_i(\Delta_{ini}) - t_{i-1}(\Delta_{ini})$. Inset: distribution of waiting times considered as the difference in value of force, $\tau_F(\mathrm{N}) = F_i - F_{i-1}$. (G) Fractal analysis of the spatial distribution of the seeds of the precursors in a typical experiment (inset), showing a behavior reminiscent of a spatial Poisson process ($d_f \simeq 2$).

crease of the force, recovering the force drop albeit with a degraded macroscopic stiffness (lower slope). This alternating sequence of damage growth and elastic re-loading is reminiscent of the avalanche dynamics observed in driven disordered elastic systems [40–42]. We construct the mechanical response of the specimen (in red) in an equivalent force control experiment where displacement jumps (from Δ_{ini} to Δ_{end}) at constant force correspond to a cascade of damage growth, also called an avalanche (Fig. 1*C*, see also SI Sec.1 and Fig. S1*A*). The precursors defined this way can be shown to be statistically similar to those that would be measured during an actual force control experiment (see SI, Sec. S4 for a numerical validation). As under force control conditions damage cascades take place at constant force, the work of the loading machine ΔW during the event can be shown to contribute equally to the increase ΔE_{el} of the elastic energy and to the dissipation ΔE_{d} by damage (see SI Sec. S1A). Hence, $\Delta E_{\mathrm{d}} = \Delta W/2 = (\Delta_{\mathrm{end}} - \Delta_{\mathrm{ini}})\, F_0/2$ and we define this quantity as the precursor size S_{global}. The evolution of S_{global} with the distance to failure $\delta = (F_{\mathrm{c}} - F)/(F_{\mathrm{c}} - F_{\mathrm{el}})$ is shown in Fig. 1*D*. The cascading dynamics and its amplification on approaching failure ($\delta \to 0$) observed in our 2D cellular material under compression are reminiscent of the intermittent damage activity evidenced by acoustic emissions in more complex materials.

Alternatively, we can also identify and characterize the precursors at the local scale using our (time-resolved) full-field measurement of the displacement and the damage field (see SI Sec. 1C and Figs. S1*C-F* for details on the local analysis). From these quantities, we compute the field of stored elastic energy in the specimen. Considering energy balance at the local scale, we can thus determine the dissipation energy density $\rho(\vec{x}, \Delta)$ that we integrate over an avalanche $\rho(\vec{x}) = \int_{\Delta_{\mathrm{ini}}}^{\Delta_{\mathrm{end}}} \rho(\vec{x}, \Delta)\, d\Delta$

Maps of dissipation energy density $\rho(\vec{x})$ depicting the complex spatial structure of precursors are presented in Fig. 2*A*. We observe a diffuse pattern, yet containing locally well defined regions of varying intensity and size. These clusters are reminiscent of the time and space correlated structure of incremental damage events. In practice, highly correlated individual damage events can be grouped together by implementing a spatio-temporal clustering algorithm on the fields $\rho(\vec{x}, \Delta)$ recorded during $\Delta_{\mathrm{ini}} < \Delta < \Delta_{\mathrm{end}}$. This reveals the cluster-like structure of precursors, illustrated in Fig. 2*B* (see also Video S2) for the precursor shown in the second panel of Fig. 2*A*.

The energy $S_{\mathrm{local}} = \int \rho(\vec{x}) d\vec{x}$ dissipated during the cascade compares well with the precursor size S_{global} inferred from the force-displacement response, see Fig. 1*D*. It is also in good agreement with the precursor size computed using the field of dissipated energy inferred from the in-

cremental damage field, thus validating the assumption of local energy balance (see SI Sec. S2, Figs. S2D and S2E).

Statistical characterization of precursors

We now explore the properties of the damage cascades observed in our experiments. First, their spatial extent is determined from (thresholded) maps of dissipation energy density (insets of Fig. 2A). The employed threshold value ρ^* is inferred from the distribution of local dissipation densities that follows an exponential decay $P(\rho) \propto \mathrm{e}^{-\rho/\rho^*}$ (see SI Sec. S1C and Fig. S1G). We extract the characteristic length ξ from the 2D autocorrelation of thresholded dissipation map (SI Sec. S1D and Fig. S1H). The length grows with the avalanche size as $S \propto \xi^{d_\mathrm{f}}$, where $d_\mathrm{f} \simeq 1.07$ is the fractal dimension, see Fig. 2C. While cascades spread over the whole specimen (see Fig. 2A), ξ represents the spatial extent of the largest clusters constituting the cascade. Interestingly, ξ reaches the specimen size L on approaching failure, which implies an upper limit on the size of the precursors. An independent estimate of the fractal dimension of the precursors is obtained from the spatial distributions of the clusters. We identify the location of their center of mass, as illustrated on the right-end of Fig. 2B, and then compute the correlation function $C(r) \propto r^{d_\mathrm{f}}$ defined as the fraction of pairs of points whose separation is less than r [50]. This provides a fractal dimension $d_\mathrm{f} \simeq 1.15$ (see inset of Fig. 2C) compatible with the one obtained from the spatial distribution of the individual damage events.

We now seek to determine the characteristic duration of the damage cascades. We come back to the force-displacement response and explore the sequence of load drops observed within an avalanche. The precursor duration T is defined as the number of load drops (also see SI Sec. S1B and Figs. S1A and S1B). It scales with the characteristic length ξ of the precursor as $T \propto \xi^z$, see Fig. 2D, with dynamic exponent $z \simeq 0.53$.

Thus, a damage cascade is characterized by its size, its spatial extent and its duration. All three quantities are related to each other by scaling laws. The probability distribution of these quantities is studied in Fig. 2E, where we focus on the distribution $P(S)$ of precursor sizes, the other distributions $P(\xi)$ and $P(T)$ being inferred from the previous scaling laws. Considering all the precursors ($\delta \in [0,1]$) or only the ones close to localization ($\delta \in [0,0.01]$), both distributions follow a power-law statistics but with two different exponents $\beta_\mathrm{tot} \simeq 2.34$ and $\beta \simeq 1.30$, respectively. This difference results from the variations of the mean precursor size with the distance to failure (see SI Sec. S4A).

Finally, we characterize the correlations in the sequence of damage cascades. The distribution $P(\tau_\mathrm{w})$ of waiting times separating two successive damage cascades is shown in Fig. 2F. It follows an exponential law $P(\tau_\mathrm{w}) \propto \mathrm{e}^{-\tau_\mathrm{w}/\tau_\mathrm{w}^\star}$, defining a characteristic waiting time $\tau_\mathrm{w}^\star$. This result is at odd with the power-law distribution of waiting times separating acoustic events in compression experiments [19–21]. To confirm our observation, we perform additional experiments with a loading rate v_ext twice smaller. Interestingly, we also measure an exponential distribution, but with a characteristic waiting time about twice larger (see Fig. 2F). We thus replace the waiting time τ_w by the force increment τ_F separating two successive precursors, so that distributions corresponding to different loading rates collapse on a single curve, as shown on the inset of Fig. 2F. The exponential distribution of waiting time, characteristic of uncorrelated events described by a Poisson process, suggests that precursors are triggered independently from each others. This is further confirmed by the spatial distribution of the seeds (first damage event) of precursors that we define as the center of mass of the cluster appearing at $t(\Delta_{ini})$. The fractal analysis of the precursor seeds provides $C(r) \propto r^2$ a behavior reminiscent of spatially uncorrelated events (see Fig. 2G).

THEORETICAL MODELING OF COMPRESSIVE FAILURE

The statistical features of the precursors measured in our experiments strikingly remind the avalanche dynamics of elastic interfaces driven in disordered media. In these models, an elastic interface responds to a continuously increasing drive and exhibits scale free avalanches or crackling noise [40–42]. The size, spatial extent and duration of the avalanches are related by scaling laws with universal exponents that depend on the interface elasticity and its dimension. For interfaces with long-range elasticity, avalanches are formed by a set of correlated clusters that are spatially disconnected similar to damage clusters within a cascade observed in our experiments (see Fig. 2B). Taking inspiration from Weiss *et al.* [38] and using the non-local theory proposed in Dansereau *et al.* [49], we derive below an evolution equation of the damage field in the specimen for a compression test under force control conditions. This theoretical formulation sheds light on the connection with models of driven disordered elastic interfaces. We provide here the main ingredients of the derivation of the damage evolution law, the detailed calculations being presented in SI Sec. S3A-D.

First, we assume that the material behaves as an elasto-damageable solid. We thus introduce a damage field $d(\vec{x},t)$ that describes the level of damage accumulated in the specimen at the location $\vec{x}$ and time t. Damage growth is inferred from a balance of energy, by comparing two quantities: the local driving force $Y[d(\vec{x},t),t]$ which provides the rate of elastic energy released for an

incremental growth of damage, and the damage resistance $Y_c[d(\vec{x},t)]$ which provides the material resistance to damage and corresponds to the rate of energy dissipated for an incremental growth of damage. The first quantity is similar to the elastic energy release rate introduced in fracture mechanics, which drives crack propagation and is a quadratic function $Y \propto \sigma_0^2$ of the nominal compressive stress $\sigma_\circ = F/(L\,W)$ applied by the test machine [51, 52]. The damage resistance is equivalent to the fracture energy introduced in fracture mechanics. Note that in our model, Y_c depends not only on $\vec{x}$ as precursors emerge from the material inhomogeneities, but also on d as a damage event in $\vec{x}$ may change the subsequent failure resistance in the same material element. The damage then increases in the material element $\vec{x}$ if the local value of the driving force $Y(\vec{x})$ reaches the material resistance $Y_c(\vec{x})$.

To describe the damage field fluctuations resulting from the material heterogeneities, we introduce a reference damage level $d_\circ = \langle d(\vec{x},t_\circ)\rangle$ and the damage field perturbations $\Delta d(\vec{x},t) = d(\vec{x},t) - d_\circ$ over the time $\delta t = t - t_\circ \ll t_\circ$ to ensure that $\langle \Delta d(\vec{x},t)\rangle_{\vec{x}} \ll d_\circ$. The driving force and the damage resistance can then be linearized as $Y[d(\vec{x},t),\sigma_\circ] = Y_\circ(d_\circ,\sigma_\circ) + \Delta Y[\Delta d(\vec{x},t),\sigma_\circ]$ and $Y_c[d(\vec{x},t)] = Y_{c\circ}(d_\circ) + \Delta Y_c[\Delta d(\vec{x},t)]$. The zero-order equation $Y_\circ(d_\circ,\sigma_\circ) = Y_{c\circ}(d_\circ)$ provides the relationship between the reference damage level $d_\circ$ and the reference applied load $\sigma_\circ = \sigma(t_\circ)$. In the following, we investigate how the damage field perturbations $\Delta\dot{d}(\vec{x},t) \propto \Delta Y[\Delta d(\vec{x},t),\sigma_\circ] - \Delta Y_c[\Delta d(\vec{x},t)]$ evolves over time. We write the total driving force as the sum of three terms [38, 49],

$$\Delta\dot{d}(\vec{x},t) \propto \mathcal{K}(\sigma_\circ)\,[v_m(\sigma_\circ)\,t - \Delta d(\vec{x},t)] + \psi(\sigma_\circ) * [\Delta d(\vec{x},t) - \langle \Delta d\rangle_{\vec{x}}] - y_c[\vec{x}, d(\vec{x},t)]. \quad (1)$$

The first (local) term comprises the effect of the driving by the test machine, where the driving speed $v_m \propto v_{ext}$ sets the damage growth rate. Considering a pseudo-interface of position $\Delta d(\vec{x},t)$, this term acts as a rigid plate moving at a speed v_m and pulling on the interface with springs of stiffness $\mathcal{K}$ (see SI Fig. S3 for a schematic representation). The second term is non-local. It describes the interactions within the specimen, its values in $\vec{x}$ depends on the damage level $\Delta d(\vec{x},t)$ everywhere in the specimen. In practice, the kernel $\psi(\sigma_\circ)$ (provided in SI Eq. S13) describes the spatial structure of the redistribution of driving force taking place in the aftermath of an individual damage event. It decays as $\psi \propto 1/r^2$ [38, 49]. Its angular dependence is shown in Fig. 3*A* for the particular case of uni-axial compression. It exhibits a quadrupolar symmetry with non-positive regions (in blue). Hence only a fraction of the neighboring elements are reloaded in the aftermath of a damage event while the others (located above and below the damaged element) are actually unloaded. The third term represents the effect of material disorder. Its spatial average is close to zero as the contribution of the hardening $\langle \Delta Y_c\rangle_{\vec{x}} = \eta\,\langle \Delta d\rangle_{\vec{x}}$ (where η is a hardening parameter and observed in our experiments) is taken into account in the first term (see SI Sec. S2 and Figs. S2*B* and S2*C*). The presence of $d(\vec{x},t)$ as an argument of the disorder term implies that (1) is strongly non-linear, leading to the rich phenomenology that we now discuss.

Equation (1) provides a clear connection between damage evolution and disordered elastic interfaces: the accumulated damage field is analogous to a 2D elastic interface $\Delta d(\vec{x},t)$ driven at the speed v_m through a 3D disordered medium (see SI Sec. S3E, Fig. S3). As a result, damage is expected to grow through bursts characterized by scaling laws involving critical exponents reminiscent of the so-called depinning transition. As a first test of our model, we compare the theoretically predicted exponents with the one measured experimentally. Investigating the avalanches dynamics of 2D interfaces with non-positive interactions in the context of amorphous plasticity, Lin *et al.* [53, 54] predicted the exponent values $\beta = 1.51$, $d_f = 1.10$ and $z = 0.57$ that agree reasonably well with the ones measured in our experiments. Corrections to these predictions from the numerical solution of the evolution equation (1) are provided at the end of our manuscript, in section . They improve further the agreement with the experimentally measured exponents.

Despite the ability of this approach to describe the scaling behavior of precursors, we note that two important features of the damage evolution equation (1) differ from standard models of driven elastic interfaces. First, the long-range elastic interactions result in both reloading and unloading of material elements in the aftermath of a damage event. Second, a subtler but more important feature is that (1) describes a non-stationary depinning scenario culminating in a bifurcation at the localization threshold. In the following, we examine these aspects in details and discuss their implications on the damage accumulation process preceding failure.

ATYPICAL ASPECTS OF DAMAGE EVOLUTION AS A DRIVEN DISORDERED ELASTIC INTERFACE

Elastic interactions

Taking advantage of our full-field characterization of damage spreading, we determine the elastic interactions driving the collective dynamics of failure precursors from our experimental data. As the organization of the damage events into clusters follows from these interactions, we expect that it encodes their signature. Here, we focus on the damage field and in particular on the incremental damage field $\delta d(\vec{r})$ during an avalanche. Its 2D auto-

correlation function $C(\vec{\delta r}) = \langle \delta d(\vec{r}) \cdot \delta d(\vec{r} + \vec{\delta r}) \rangle_{\vec{r}}$ averaged over several avalanches is presented in Fig. 3*B*. The angular distribution (at a fixed distance) shows a clear quadrupolar symmetry similar to the re-distribution pattern of the theoretical interaction kernel (Fig. 3*A*). Remarkably, the correlation along the horizontal axis where the reloading is maximal decays as $C(\delta r) \propto 1/\delta r^2$ (see Fig. 3*C*), a behavior also in line with the theoretical predictions of the elastic kernel (SI Eq. S13). These observations support further the evolution equation (1), and in particular, the interaction kernel ψ predicted by our damage model.

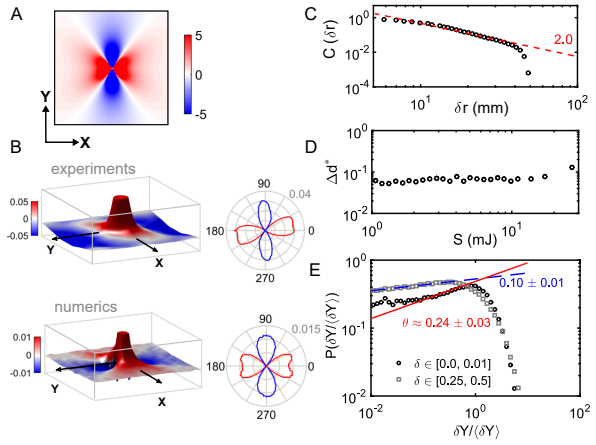

FIG. 3. (A) Angular distribution of the long-range interaction kernel derived theoretically for the case of uni-axial compression. (B) 2D auto-correlation map of the incremental damage field of precursors and angular distribution of the correlations at a fixed distance as obtained from the experiments and the numerical simulations. (C) Variations of the correlation function of the incremental damage field with distance along the horizontal x-axis and comparison with the scaling $\psi \propto 1/\delta r^2$ of the theoretical interaction kernel (dashed line). (D) Variations of the depth Δd^* of the damage cascade with the cascade size S. (E) Distribution of the local distance to failure $\delta Y(\vec{x})$ close and far from failure.

The presence of an unloading region in the interaction kernel has several important implications. First, the characteristic damage increment Δd^* of a precursor - defined as the average damage increment over all the damaging material elements of a cascade - is expected to be constant (as discussed in SI Sec. S4A), irrespective of the precursor size S [53]. This prediction is verified in Fig. 3*D*. In other words, the depth of damage cascades is constant, at odds with the behavior of driven elastic interfaces with positive interactions for which the depth of avalanches scales with their size. Another crucial, yet more subtle difference relates to the distribution of net driving force $\delta Y(\vec{x}) = Y_c(\vec{x}) - Y(\vec{x})$ that controls the (marginal) stability of the specimen. $\delta Y(\vec{x}) > 0$ provides the increment of driving force required for triggering damage. Its distribution, computed over all the material elements, is expected to scale as $P(\delta Y) \propto \delta Y^\theta$ [53, 55, 56]. Positive interactions lead to $\theta = 0$, pointing out the presence of a finite number of material elements close to failure. On the contrary, the number of elements close to failure vanishes for sign-changing interactions, leading to $\theta > 0$. The experimental determination of the exponent θ is quite challenging, as it requires a priori the knowledge of the material disorder. In practice, we circumvent this difficulty by computing the driving force $Y(\vec{x}, t)$ (according to SI Eq.S4) at each time step for each material element and determine $Y_c[d(\vec{x}, t)]$ retrospectively from the value of $Y(\vec{x}, t)$ when the material element damages (see SI Sec. 2 and Fig. S2*A* for details on the method). Figure 3*E* shows the distribution $P(\delta Y/\langle \delta Y \rangle)$ close and far from localization. In both cases, we measure a positive exponent $\theta > 0$, a particularly non-trivial property that comes in support of the proposed model. Interestingly, θ increases as the specimen approaches failure, a feature that possibly arises from the non-stationary nature of the evolution equation (1). A similar trend has been reported in direct simulations of sheared amorphous solids that are also characterized by sign-changing interactions [55, 57].

Divergence of precursors

We now come back on the observations made in Fig. 1*D* and Fig. 2*A* of an increase of the size and the spatial extent of precursors close to failure. As shown in Fig. 4*A*, the average precursor size increases as a power-law with the distance to failure, $\langle S \rangle \sim 1/\delta^{-\alpha}$ where $\alpha \simeq 0.57$. Following the scaling relations $S \propto \xi^{d_f}$ and $T \propto \xi^z$, the associated length and time scales then also diverge on approaching failure. This is confirmed by the variations of the precursor spatial extent directly measured from our local analysis (see SI Sec.1D) in the inset of Fig. 4*A*.

Notably, the activity rate dN_S/dt i.e., the number of cascades per interval of time is rather constant during damage accumulation, see Fig. 4*B*. This is in line with our previous observation of an exponential distribution of waiting times, supporting further that precursors emerge from a (random) Poisson process. As the dissipation rate dE_d/dt during the intermittent damage evolution writes as the product of the average precursor size with the precursor rate, $dE_d/dt = \langle S \rangle dN_S/dt$, we obtain $dE_d/dt \propto 1/\delta^{-\alpha}$. As explained in the next section, the divergence of the dissipation rate on approaching peak load is the hallmark of damage localization, a feature that results from the loss of stability of homogeneously damaged specimen. To further test this idea, we reanalyze our data considering the actual displacement imposed conditions that also gives rise to damage localization at peak load. The dissipation rate then writes as the product of the average load drop size $\langle A \rangle$ with their activity rate dN_A/dt (refer to SI Sec.1B and Fig.S1*B* for the definition of precursors under displacement imposed

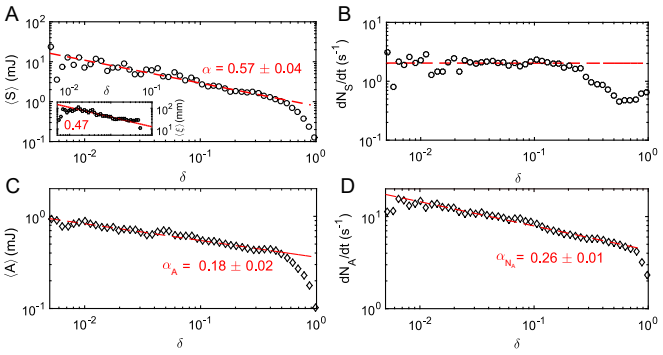

FIG. 4. Variation with distance to failure of (A) the average precursor size $\langle S \rangle$, the average spatial extent of precursors $\langle \xi \rangle$ in the inset, (B) the activity rate dN_S/dt, (C) the average size of load drop events $\langle A \rangle$ and (D) the event activity rate dN_A/dt. While S and dN_S/dt characterize the intermittent damage activity under force controlled conditions, A and dN_A/dt are relevant for displacement imposed conditions. The product of both quantities $dE_d/dt = \langle S \rangle \, dN_S/dt = \langle A \rangle \, dN_A/dt$ provides the dissipation rate that also diverges as $dE_d/dt \sim \delta^{-\alpha}$ with $\alpha = 1/2$.

loading conditions). We observe that both load drops $\langle A \rangle \propto \delta^{-\alpha_A}$ and precursor rate $dN_A/dt \propto \delta^{-\alpha_{N_A}}$ diverge on approaching localization, see Fig. 4*C* and *D*. The exponent $\alpha = \alpha_A + \alpha_{N_A} \simeq 0.44$ characterizing the dissipation rate under displacement imposed conditions is close to 1/2, as expected and accounts for the numerical observations of Girard *et al.* [31] who reported $dE_d/dt \propto \delta^{-0.4}$. On the contrary, standard stationary models of driven elastic interfaces would provide $\alpha = 0$.

DAMAGE LOCALIZATION : DEPINNING TRANSITION OR STANDARD BIFURCATION ?

To discuss in depth the nature of compressive failure by damage localization, we would like to come back to the proposed model. We focus on the non-stationary aspects of (1), namely the stiffness $\mathcal{K}$ and the driving speed v_m that are given by the following expressions:

$$\begin{aligned} \mathcal{K}(\sigma_\circ) &= \left. \frac{\partial (Y_{c\circ} - Y_\circ)}{\partial d_\circ} \right|_{\sigma_\circ} \\ v_m(\sigma_\circ) &= v_{ext} \left(\frac{\partial Y_\circ / \partial \sigma_\circ|_{d_\circ}}{\mathcal{K}(\sigma_\circ)} \right). \end{aligned} \tag{2}$$

$\mathcal{K}$ controls the stability of the damage evolution. Indeed, a negative value of $\mathcal{K}$ implies that the net driving force $Y - Y_c$ increases with the damage level, leading to its unstable growth and thus failure. It turns out that $\mathcal{K}$ goes to zero on approaching peak load (see SI Sec. S3F), in line with the stability condition under force controlled conditions. The driving speed v_m is inversely proportional to $\mathcal{K}$ and hence goes to infinity. A linear expansion of the damage evolution equation close to peak load $\sigma_\circ < \sigma_c$ (see SI Sec. S3G), provides the asymptotic behavior of the damage growth rate $\dot{\Delta d} \sim 1/\sqrt{\delta}$. As $\dot{\Delta d} \propto v_m$, owing to (2) we obtain $v_m \sim 1/\sqrt{\delta}$ and thus $\mathcal{K} \sim \sqrt{\delta}$.

What are then the consequences of the divergence of the speed of the pseudo-interface at peak load ? As the rate of dissipated energy is controlled by the damage growth rate, one expects $dE_d/dt \propto 1/\sqrt{\delta}$. Considering the intermittency of damage evolution, the dissipation rate writes as the product of the precursors' size with the precursors' rate, $dE_d/dt = \langle S \rangle \, dN_S/dt$. As dN_S/dt remains constant during the experiment (Fig. 4*B*), a feature expected for disordered elastic interfaces, it follows that $\langle S \rangle \sim 1/\sqrt{\delta}$, a prediction that adequately captures our experimental observations.

The implication of our finding are clear: the divergence of the size of the precursors close to failure, and hence the divergence of the length scale and time scale of the fluctuations, result from the divergence of the dissipation rate, a hallmark of standard bifurcation. As such, this behavior is reminiscent of the unstable growth of damage at peak load and thus of the loss of stability of the homogeneous material response, a behavior that has no relationship with critical transitions.

To further support this claim, we rewrite the damage evolution law (1) using the new variable $\underset{\sim}{d}(\vec{x}) = d(\vec{x}) \sqrt{\delta}$. The obtained expression ensures a straightforward connection with standard (stationary) depinning models [40, 42]:

$$\begin{aligned} \dot{\underset{\sim}{\Delta d}} \propto \mathcal{K}_0 \left[v_{m0} \, t - \Delta \underset{\sim}{d}(\vec{x}, t) \right] + \\ \psi(d_\circ \sqrt{\delta})/\sqrt{\delta} * [\Delta \underset{\sim}{d}(\vec{x}, t) - \langle \Delta \underset{\sim}{d} \rangle_{\vec{x}}] - y_c[\vec{x}, \underset{\sim}{d}(\vec{x}, t)]. \end{aligned} \tag{3}$$

Under this form, the evolution equation displays both a constant stiffness $\mathcal{K}_0 = \mathcal{K}/\sqrt{\delta}$ and a constant driving speed $v_{m0} = v_m \sqrt{\delta}$. The normalized damage field $\underset{\sim}{d}$ behaves as an elastic interface driven at constant finite speed during the whole damage accumulation regime. As a result, the specimen remains at a fixed distance to the critical point that corresponds to the limit $v_{m0} \to 0$ and $\mathcal{K}_0 \to 0$. Our conclusions are in stark contrast with a depinning scenario where the divergence of the precursory activity results from the interpretation of compressive failure as a critical transition and the evolution of the specimen towards this critical point. In other words, the increasing applied load drives the specimen towards instability without driving it towards more criticality.

We now would like to highlight the strategic value of our findings to structural health monitoring. In our theoretical description of compressive failure, the evolution of precursors is described by robust scaling laws that are independent of the material properties and the loading conditions. In particular, as they apply for both force and displacement driven experiments, they serve as early

warning signals of impending failure.

FAILURE PREDICTION FROM PRECURSORY ACTIVITY

We now harness the scaling behavior of the precursors and bring an experimental proof of concept of their predictive power by inferring the residual life-time of our specimen. We perform a retrospective failure prediction using the cascade size S measured during the damage accumulation regime. To do so, we follow the idea of Anifrani *et al.* [58] and use the methodology proposed by Mayya *et al.* [59]. Considering a time-series of measured precursory activity for the equivalent force-controlled experiment, the normalized distance to failure here writes as $\delta = (t_c - t)/t_c$ where $t = 0$ corresponds to $F = F_{el}$ and $t = t_c$ corresponds to $F = F_c$. We rewrite the scaling law for the cascade size variations as

$$\langle S \rangle = S_0/\sqrt{t_c - t} \tag{4}$$

where S_0 is a constant. Re-arranging the terms, we obtain $\langle S \rangle^2 t = \langle S \rangle^2 t_c + S_0$, an expression that can be used for performing a linear-regression of our experimental data set (t, S) shown in Fig. 5*A*. The average size of the precursors is obtained over a non-overlapping time window of 10 s. The prediction is made at time t_{cur} so that only the precursors recorded at time $t < t_{cur}$ can be used for the prediction. Note, however, that we only use a short period (here 100 s) before t_{cur} to make the prediction.

The linear regression provides t_c^{pred} that is shown in Fig. 5*B* as a function of t_{cur}. As shown in inset, the error on the predicted failure time reduces as the prediction is made closer to the actual failure time t_c. The prediction lies within 10 % error when the prediction is made in the last 25 % of the total lifetime. Note that the same methodology can be implemented using the duration or the rate of events (under displacement controlled conditions only), thus providing several independent measurements to forecast final failure. Interestingly, the predictions are conservative by providing shorter residual lifetime than the actual one. Importantly, the proposed methodology does not require monitoring from the beginning of the damage accumulation phase.

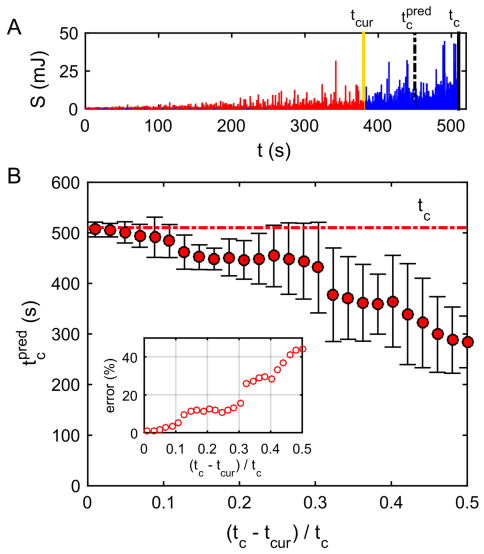

FIG. 5. (A)Time series data of failure precursors obtained during the compression test and data available for prediction (red) at t_{cur}. (B) Variation of the predicted remaining lifetime at different instances t_{cur} represented as a fraction of the time to failure. The error bars provide intervals with 90% confidence levels. Inset : Error on the predicted remaining lifetime.

NUMERICAL SOLUTION OF THE DAMAGE EVOLUTION EQUATION

To conclusively validate our interpretation of the non-stationary avalanche dynamics preceding compressive failure, we numerically solve the damage evolution equation (1) using a 2D cellular automata (see Materials and Methods) for both force (SI Sec. S4A) and displacement (SI Sec. S4B) control conditions. We recover that intermittent damage accumulation culminates in a bifurcation that manifests as the emergence of a localization band at peak load (SI Figs. S4*A-B* & S5*A-B*). The exponents characterizing the damage cascades are measured numerically (SI Figs. S4*C-J* & S5*C-J*) using the methods employed for analyzing the experimental data, thus allowing for a systematic comparison with the statistical features of the precursors measured experimentally. Numerical and experimental exponents are provided in Table II. We also proceed to a comparison with exponent values reported in the literature (see SI Table S2). The good agreement supports our theoretical framework as an adequate description. Importantly, the similarities between the statistics in force and equivalent-force control validate our method of reconstruction of the precursors from our experimental data set and interpretation of failure built from the analyses. We also verify numerically the method employed to characterize the elastic interactions from the incremental damage field in Fig.3*B*.

IMPLICATIONS OF A NON-STATIONARY DEPINNING SCENARIO

Our experimental investigation of the intermittent damage activity preceding failure encompasses the issue of damage localization and the behavior of driven disordered elastic interfaces with sign-changing interactions. Notably, the marginal stability exponent θ, a di-

TABLE I. Exponents from experiments and numerical model.

	Definition	Experiments	Simulations[†]
d_{f}	$S \propto \xi^{d_{\mathrm{f}}}$	1.07 ± 0.07	1.15
z	$T \propto \xi^{z}$	0.53 ± 0.11	0.62
θ	$P(\delta Y) \propto \delta Y^{\theta}$	0.24 ± 0.03	0.35 (0.18)
β	$P(S) \propto S^{-\beta}$	1.30 ± 0.11	1.36 (1.34)
α	$S \propto \delta^{-\alpha}$	0.57 ± 0.04	0.48 (0.60)
z/d_{f}	$T \propto S^{z/d_{\mathrm{f}}}$	0.49 ± 0.14	0.53 (0.64)
β_{tot}	$\beta_{tot} = \beta + \frac{2-\beta}{\alpha}$	2.32 ± 0.18	2.2 (2.13)

[†]Values in brackets are from equivalent force control scenario.

rect signature of such interactions, was shown here to be an essential feature of the compressive failure of elasto-damageable solids, while till date it had only been used in the context of amorphous plasticity. In addition, by characterizing the damage precursors in terms of dissipated mechanical energy, we showed that acoustic bursts by themselves cannot be considered as avalanches. The scaling laws characterizing the acoustic precursors are quite different from those of the damage cascades evidenced in our work and they are most likely reminiscent of the clusters constituting the avalanches rather than the avalanches themselves. Yet, our work constitutes a first step towards the quantitative understanding of the time-series record of acoustic emission preceding compressive failure. Consequently, the ideas resulting from this study could also be relevant for deciphering earthquake statistics.

The mapping of damage spreading during compressive failure to the driving of a disordered elastic interface meeting an instability paves the way for a better understanding of bifurcation phenomena in presence of disorder. In particular, the ideas developed in the context of compressive failure could be relevant to understand the relationship between intermittent plastic flow and shear banding in amorphous solids, where the nature of the yielding transition and the localization has been vigorously debated these recent years [53, 57, 60]. Last but not the least, unraveling the complex dynamics of precursors has opened perspectives for the design of physics-based quantitative tools of structural health monitoring.

In summary, we investigated experimentally how criticality meets bifurcation in compressive failure of disordered solids. We characterized the non-stationary statistics of the damage cascades observed during the damage accumulation regime prior localization. We then derived from continuum mechanics an evolution equation of the damage field that was shown to account quantitatively for all the scaling properties measured experimentally. The avalanche-dynamics of damage growth was thus shown to be reminiscent of a non-stationary depinning scenario that reconciles two contrasting approaches used so far to describe compressive failure, namely standard bifurcation and critical transition. Ultimately, precursors have been shown to be merely the by-products of the progressive loss of stability of the specimen as it approaches localization. Contrary to the critical transition scenario, specimens driven towards failure stay at a fixed distance to criticality. Nevertheless, the evolution of the statistical features of precursors can be harnessed to anticipate and even predict the forthcoming failure.

Materials and Methods

Experimental set-up

Our system consists of a hexagonal packing of about 1500 soft cylinders placed in a transparent Plexiglas box of dimensions 205mm × 170mm × 30mm, as shown in Fig. 1*A*. The cylinders are 25 mm long with a 5mm diameter. Displacement loading is applied to the upper layer through a Plexiglas beam using an AG-X Shimadzu test machine. The force experienced by the specimen is measured using a 10kN load cell and sampled at a rate of 100Hz. During the test, images are recorded every 0.1 seconds from the lateral side of the box, using a Baumer HXC20 camera with a resolution of 2048 × 1088 pixels. Precursory activity recorded during ten experiments with loading rate of 2mm/min and two experiments with loading rate of 1mm/min were analyzed to determine the exponents of the power-law relations.

Tracking damage evolution

The continuous image acquisition allows for the tracking of both the displacement and deformation (here used to define damage) of the individual cells. To resolve the damage cascades from the image stack, we refer to the macroscopic response where an equivalent force control scenario is constructed from the sequence of load drops. We thus obtain a temporal resolution of damage evolution as cascades whose start and end are marked by $t(\Delta_{\mathrm{ini}})$ and $t(\Delta_{\mathrm{end}})$, respectively. The locations of damage evolution in the image stack corresponding to cascades are then grouped based on their connectivity (26-connected neighborhood). This procedure provides a space-time dissipation map of failure precursors composed of a series of highly correlated clusters.

Numerical modeling of intermittent damage evolution and localization

To solve the damage evolution equation under quasi-static loading conditions, we adopt the procedure described in Berthier et al. [43]. We consider a heteroge-

neous field of damage resistance $Y_c[d(\vec{x},t)]$ that evolves with damage level $d(\vec{x},t)$ following the linear hardening law $Y_{c\circ} = Y_c^{\circ}(1+\eta d_\circ)$, where η is the hardening coefficient. The stress (strain) is gradually increased until the damage criterion is fulfilled for one of the elements $\vec{x} = \vec{x}_0$. The damage is increased locally and the values of driving force $Y(\vec{x}_0,t)$ and resistance $Y_c(\vec{x}_0)$ are updated. The non-local redistribution of driving force given by the term containing the kernel $\psi(d_\circ)$ may then trigger a cascade of damaging events as the reloading can fulfill damage criterion of other elements. The cascade stops when damage in all elements is stable following which, we increase the stress (strain) again.

The reader is invited to refer to the Supplementary Information for the details of the local analyses of cascades, theoretical modeling of damage evolution, analogy to elastic interface as well as the numerical modeling.

The authors gratefully acknowledge financial support from Sorbonne Université through the Emergence grant for the research project, *From damage spreading to failure in quasi-brittle materials* as well as CNRS and Satt-Lutech through the tech transfer project, *Development of a technology of predictive maintenance for materials and structures under compression.*

* Current address : Arnold-Sommerfeld-Center for Theoretical Physics and Center for NanoScience, Ludwig-Maximilians-Universität München, D-80333 München, Germany

† laurent.ponson@upmc.fr

[1] J. Koivisto, M. Ovaska, A. Miksic, L. Laurson, and M. J. Alava, Predicting sample lifetimes in creep fracture of heterogeneous materials, Physical Review E **94**, 023002 (2016).

[2] V. Kádár, G. Pál, and F. Kun, Record statistics of bursts signals the onset of acceleration towards failure, Scientific reports **10**, 1 (2020).

[3] S. Biswas, D. Fernandez Castellanos, and M. Zaiser, Prediction of creep failure time using machine learning, Scientific Reports **10**, 1 (2020).

[4] W. Debski, S. Pradhan, and A. Hansen, Criterion for imminent failure during loading—discrete element method analysis, Frontiers in Physics **9**, 223 (2021).

[5] M. Ashby and C. Sammis, The damage mechanics of brittle solids in compression, Pure and Applied Geophysics **133**, 489 (1990).

[6] D. Lockner, J. Byerlee, V. Kuksenko, A. Ponomarev, and A. Sidorin, Quasi-static fault growth and shear fracture energy in granite, Nature **350**, 39 (1991).

[7] M. Kachanov, Elastic solids with many cracks: a simple method of analysis, International Journal of Solids and Structures **23**, 23 (1987).

[8] J. Mazars and G. Pijaudier-Cabot, Continuum damage theory—application to concrete, Journal of engineering mechanics **115**, 345 (1989).

[9] J. Fortin, S. Stanchits, G. Dresen, and Y. Guéguen, Acoustic emission and velocities associated with the formation of compaction bands in sandstone, J. Geophys. Res. Solid Earth **111** (2006).

[10] J. Fortin, S. Stanchits, G. Dresen, and Y. Gueguen, Acoustic emissions monitoring during inelastic deformation of porous sandstone: comparison of three modes of deformation, Pure and Applied Geophysics **166**, 823 (2009).

[11] C. Manzato, A. Shekhawat, P. K. V. V. Nukala, M. J. Alava, J. P. Sethna, and S. Zapperi, Fracture strength of disordered media: Universality, interactions, and tail asymptotics, Phys. Rev. Lett. **108**, 065504 (2012).

[12] C. Manzato, M. J. Alava, and S. Zapperi, Damage accumulation in quasibrittle fracture, Phys. Rev. E **90**, 012408 (2014).

[13] Y. Tal, B. Evans, and U. Mok, Direct observations of damage during unconfined brittle failure of carrara marble, J. Geophys. Res. Solid Earth **121**, 1584 (2016).

[14] J. W. Rudnicki and J. Rice, Conditions for the localization of deformation in pressure-sensitive dilatant materials, Journal of the Mechanics and Physics of Solids **23**, 371 (1975).

[15] W. A. Olsson, Theoretical and experimental investigation of compaction bands in porous rock, J. Geophys. Res. Solid Earth **104**, 7219 (1999).

[16] D. Lockner, The role of acoustic emission in the study of rock fracture, in *International Journal of Rock Mechanics and Mining Sciences & Geomechanics Abstracts*, Vol. 30 (Elsevier, 1993) pp. 883–899.

[17] A. Petri, G. Paparo, A. Vespignani, A. Alippi, and M. Costantini, Experimental evidence for critical dynamics in microfracturing processes, Phys. Rev. Lett. **73**, 3423 (1994).

[18] S. Deschanel, L. Vanel, G. Vigier, N. Godin, and S. Ciliberto, Statistical properties of microcracking in polyurethane foams under tensile test, influence of temperature and density, Int. J. Frac. **140**, 87 (2006).

[19] J. Davidsen, S. Stanchits, and G. Dresen, Scaling and universality in rock fracture, Phys. Rev. Lett. **98**, 125502 (2007).

[20] J. Rosti, X. Illa, J. Koivisto, and M. J. Alava, Crackling noise and its dynamics in fracture of disordered media, J. Phys. D: Appl. Phys. **42**, 214013 (2009).

[21] J. Baró, Á. Corral, X. Illa, A. Planes, E. K. Salje, W. Schranz, D. E. Soto-Parra, and E. Vives, Statistical similarity between the compression of a porous material and earthquakes, Phys. Rev. Lett. **110**, 088702 (2013).

[22] P. Castillo-Villa, J. Baro, A. Planes, E. K. H. Salje, P. Sellappan, W. M. Kriven, and E. Vives, Crackling noise during failure of alumina under compression: The effect of porosity, J. Phys. Cond. Mat. **25**, 292202 (2013).

[23] J. Baró, K. A. Dahmen, J. Davidsen, A. Planes, P. O. Castillo, G. F. Nataf, E. K. Salje, and E. Vives, Experimental evidence of accelerated seismic release without critical failure in acoustic emissions of compressed nanoporous materials, Phys. Rev. Lett. **120**, 245501 (2018).

[24] C.-C. Vu, D. Amitrano, O. Plé, and J. Weiss, Compressive failure as a critical transition: Experimental evidence and mapping onto the universality class of depinning, Phys. Rev. Lett. **122**, 015502 (2019).

[25] D. Sornette, Sweeping of an instability: an alternative to self-organized criticality to get power laws without parameter tuning, J. Phys. I **4**, 209 (1994).

[26] S. Zapperi, P. Ray, H. E. Stanley, and A. Vespignani, First-order transition in the breakdown of disordered media, Phys. Rev. Lett. **78**, 1408 (1997).

[27] S. Zapperi, A. Vespignani, and H. E. Stanley, Plasticity and avalanche behaviour in microfracturing phenomena, Nature **388**, 658 (1997).

[28] D. Sornette, Predictability of catastrophic events: Material rupture, earthquakes, turbulence, financial crashes, and human birth, Proceedings of the National Academy of Sciences **99**, 2522 (2002).

[29] H. B. da Rocha and L. Truskinovsky, Rigidity-controlled crossover: From spinodal to critical failure, Physical Review Letters **124**, 015501 (2020).

[30] A. Guarino, A. Garcimartin, and S. Ciliberto, An experimental test of the critical behaviour of fracture precursors, Eur. Phys. J. B **6**, 13 (1998).

[31] L. Girard, D. Amitrano, and J. Weiss, Failure as a critical phenomenon in a progressive damage model, Journal of Statistical Mechanics: Theory and Experiment **2010**, P01013 (2010).

[32] F. Kun, I. Varga, S. Lennartz-Sassinek, and I. G. Main, Rupture cascades in a discrete element model of a porous sedimentary rock, Phys. Rev. Lett. **112**, 165501 (2014).

[33] N. Kandula, B. Cordonnier, E. Boller, J. Weiss, D. K. Dysthe, and F. Renard, Dynamics of microscale precursors during brittle compressive failure in carrara marble, J. Geophys. Res. Solid Earth **124**, 6121 (2019).

[34] S. Roux, A. Hansen, H. Herrmann, and E. Guyon, Rupture of heterogeneous media in the limit of infinite disorder, Journal of statistical physics **52**, 237 (1988).

[35] A. Delaplace, G. Pijaudier-Cabot, and S. Roux, Progressive damage in discrete models and consequences on continuum modelling, Journal of the Mechanics and Physics of Solids **44**, 99 (1996).

[36] A. Garcimartin, A. Guarino, L. Bellon, and S. Ciliberto, Statistical properties of fracture precursors, Phys. Rev. Lett. **79**, 3202 (1997).

[37] Y. Moreno, J. B. Gòmez, and A. F. Pacheco, Fracture and second-order phase transitions, Phys. Rev. Lett. **85**, 2865 (2000).

[38] J. Weiss, L. Girard, F. Gimbert, D. Amitrano, and D. Vandembroucq, (finite) statistical size effects on compressive strength, Proceedings of the National Academy of Sciences **111**, 6231 (2014).

[39] F. Renard, J. Weiss, J. Mathiesen, Y. Ben-Zion, N. Kandula, and B. Cordonnier, Critical evolution of damage toward system-size failure in crystalline rock, J. Geophys. Res. Solid Earth **123**, 1969 (2018).

[40] A. L. Barabási and H. E. Stanley, *Fractal concepts in surface growth* (Cambridge University Press, 1995).

[41] J. Sethna, K. Dahmen, and C. R. Myers, Crackling noise, Nature **410**, 242 (2001).

[42] K. J. Wiese, Theory and experiments for disordered elastic manifolds, depinning, avalanches, and sandpiles, arXiv preprint arXiv:2102.01215 **.** (2021).

[43] E. Berthier, A. Mayya, and L. Ponson, Damage spreading in quasi-brittle disordered solids: Ii. what the statistics of precursors teach us about compressive failure, Journal of the Mechanics and Physics of Solids **162**, 104826 (2022).

[44] C. Poirier, M. Ammi, D. Bideau, and J. P. Troadec, Experimental study of the geometrical effects in the localization of deformation, Phys. Rev. Lett. **68**, 216 (1992).

[45] F. Renard, J. McBeck, N. Kandula, B. Cordonnier, P. Meakin, and Y. Ben-Zion, Volumetric and shear processes in crystalline rock approaching faulting, Proceedings of the National Academy of Sciences **116**, 16234 (2019).

[46] A. Cartwright-Taylor, I. G. Main, I. B. Butler, F. Fusseis, M. Flynn, and A. King, Catastrophic failure: How and when? insights from 4-d in situ x-ray microtomography, J. Geophys. Res. Solid Earth **125**, e2020JB019642 (2020).

[47] S. Lennartz-Sassinek, I. Main, M. Zaiser, and C. Graham, Acceleration and localization of subcritical crack growth in a natural composite material, Phys. Rev. E **90**, 052401 (2014).

[48] J. Davidsen, G. Kwiatek, E.-M. Charalampidou, T. Goebel, S. Stanchits, M. Rück, and G. Dresen, Triggering processes in rock fracture, Phys. Rev. Lett. **119**, 068501 (2017).

[49] V. Dansereau, V. Démery, E. Berthier, J. Weiss, and L. Ponson, Collective damage growth controls fault orientation in quasibrittle compressive failure, Phys. Rev. Lett. **122**, 085501 (2019).

[50] H. Hentschel and I. Procaccia, The infinite number of generalized dimensions of fractals and strange attractors, Physica D: Nonlinear Phenomena **8**, 435 (1983).

[51] B. Lawn, *Fracture of brittle solids* (Cambridge University Press, 1993).

[52] E. Berthier, *Quasi-brittle failure of heterogeneous materials : Damage statistics and localization*, Ph.D. thesis, Université Pierre et Marie Curie (2015).

[53] J. Lin, E. Lerner, A. Rosso, and M. Wyart, Scaling description of the yielding transition in soft amorphous solids at zero temperature, Proceedings of the National Academy of Sciences **111**, 14382 (2014).

[54] J. Lin and M. Wyart, Mean-field description of plastic flow in amorphous solids, Phys. Rev. X **6**, 011005 (2016).

[55] J. Lin, T. Gueudré, A. Rosso, and M. Wyart, Criticality in the approach to failure in amorphous solids, Phys. Rev. Lett. **115**, 168001 (2015).

[56] Z. Budrikis, D. F. Castellanos, S. Sandfeld, M. Zaiser, and S. Zapperi, Universal features of amorphous plasticity, Nature communications **8**, 1 (2017).

[57] M. Ozawa, L. Berthier, G. Biroli, A. Rosso, and G. Tarjus, Random critical point separates brittle and ductile yielding transitions in amorphous materials, Proceedings of the National Academy of Sciences **115**, 6656 (2018).

[58] J.-C. Anifrani, C. Le Floc'h, D. Sornette, and B. Souillard, Universal log-periodic correction to renormalization group scaling for rupture stress prediction from acoustic emissions, Journal de Physique I **5**, 631 (1995).

[59] A. Mayya, E. Berthier, and L. Ponson, Procédé et dispositif d'analyse d'une structure. french patent application fr2002824 (2020).

[60] G. Parisi, I. Procaccia, C. Rainone, and M. Singh, Shear bands as manifestation of a criticality in yielding amorphous solids, Proceedings of the National Academy of Sciences **114**, 5577 (2017).

SUPPLEMENTARY INFORMATION

TABLE I. List of notations used in the manuscript and supplementary information

L, H, b	: Length, height and thickness of the specimen
F	: Force experienced by the specimen as recorded at the macroscopic scale
Δ	: Applied displacement by the loading machine during the experiment
E	: Elastic modulus of the specimen
ν	: Poisson ratio of the specimen
σ_{ext}	: Nominal stress experienced by the specimen during the experiment
ϵ_{ext}	: Nominal strain experienced by the specimen solid during the experiment
W, ΔW	: Input work and incremental input work by the loading machine
E_{el}, ΔE_{el}	: Total elastic energy and incremental elastic energy in the specimen corresponding to input work
E_d, ΔE_d	: Total energy dissipated and incremental dissipation during damage growth in the specimen
$_{\text{global, local}}$	: Subscripts specifying the mode of analysis - macroscopic response (global) and at the cells (local)
Δ_{ini}, Δ_{end}	: Values of displacement corresponding to the start and end of the damage cascade in equivalent force control scenario
δ	: Normalized distance to failure
ρ	: Dissipation energy density of the material element
ρ_{th}	: Thresholded value of the dissipation energy density of the material element
S	: Size of the damage cascade
ξ	: Spatial extent of the damage cascade
T	: Duration of the damage cascade
A	: Size of the load drops
dN_S/dt	: Activity rate of the cascades
dN_A/dt	: Activity rate of the load drops
τ_w, τ_F	: Waiting time between the cascades in terms of time and force
Δd^*	: Characteristic damage value of the cascades
d_{f}	: Fractal dimension
z	: Dynamic exponent
θ	: Exponent characterizing the marginal stability
β	: Exponent characterizing the decay of distribution of cascade size, S close to failure
β_{tot}	: Exponent characterizing the decay of the stress-integrated distribution of cascade size, S
α	: Exponent characterizing the divergence of size of precursors on the approach to failure
$d_\circ$	: Average damage level in the specimen
$\delta d(\vec{x})$	: Perturbations to the mean damage level whose average over the field is zero
$d(\vec{x}, t)$	: Local damage level at any time t during the experiment
$\Delta d(\vec{x}, t)$	: Incremental damage from $d_\circ$ at site $\vec{x}$ during the experiment
$Y[\vec{x}, d(\vec{x}, t), X_0]$	: Local damage driving force determined for a fixed external driving parameter(stress or strain), X_0.
$\psi(d_\circ)$	: Non-local interaction kernel describing the redistribution of elastic energy after an incremental damage event
$Y_c[\vec{x}, d(\vec{x}, t)]$	: Local damage resistance corresponding to the threshold for damage growth
η	: Damage hardening parameter characterizing the variation of damage resistance with damage level
$y_c[\vec{x}, d(\vec{x}, t)]$	: Fluctuations in the field of damage resistance visited by the damage like elastic interface
$\delta Y(\vec{x})$	: Distance to local failure, i.e., incremental damage in line with energy based damage criterion
$\mathcal{K}$	: Stiffness of springs driving the elastic interface describing the global stability of damage evolution
v_{m}	: Velocity of the rigid plate that is connected to the pseudo-interface
$\delta d_\circ$	: Incremental damage that occurs whenever the damage criterion is satisfied
$\langle\,\rangle$	: mean of the enclosed quantity

Experimental precursors from an equivalent force control scenario

The macroscopic response of the specimen under displacement controlled loading conditions comprises intermittently occurring load drops during which damage grows, followed by elastic reloading phases. Here, we construct an equivalent force control scenario (cyan curve in Fig. 1*A*) from the displacement control experiment (blue curve). As a result, damage evolution is interpreted as a micro-instability manifesting as a jump of displacement from Δ_{ini} to Δ_{end} at constant force, wherein distinct damage events (force drops outlined in red) are separated by silent times corresponding to elastic re-loading. The macroscopic response is thus reconstructed as a sequence of force plateaus followed by elastic reloading.

Precursors size at the global scale

For the equivalent force control scenario, the incremental work done by the external force during silent damage periods (for $\Delta \leq \Delta_{\text{ini}}$ and $\Delta_{\text{end}} \leq \Delta$) is converted into elastic energy, $dW = dE_{\text{el}} = \frac{1}{2}F\Delta$. During the equivalent force control cascade (for $\Delta_{\text{ini}} \leq \Delta \leq \Delta_{\text{end}}$), only a part of the incremental work $dW = F(\Delta_{\text{end}} - \Delta_{\text{ini}})$is stored in the material as elastic energy. The remaining part $\Delta E_{\text{d}} = \Delta W - \Delta E_{\text{el}} = \Delta W/2$ is dissipated through damage. This quantity defines the avalanche size S_{global} at the global (macroscopic) scale.

Precursors duration and damage events within a cascade

The duration of the force plateau is dependent on the cross-head velocity of the loading machine. Thus, it cannot be used to define the intrinsic duration T of a precursor. To determine the duration of a cascade of damage events, we focus on the load drops observed during the force-plateau (Fig. 1*B*). The intermittent load drops are reminiscent of the individual events within a cascade of damage growth during a force controlled experiment. Taking τ as the characteristic duration for these damage events, the duration of a cascade writes as $T = N\tau$, where N is the number of load drops during the cascade. Following this framework, we consider the magnitude of the load drops, denoted by A, as the size of the damage events during the cascade. Only the load drops of magnitude greater than 0.1 N are considered as individual events. As damage events manifest as highly correlated spatio-temporal clusters, load drops are expected to be macroscopic manifestation of the clusters of correlated individual damage events observed at the local scale, see Fig. 2B in the main article.

Precursors size at the local scale

The continuous image acquisition during the experiment allows for the tracking of both the location and the deformation of individual cells, which are then used to analyze the spatio-temporal structure of damage cascades at the local scale. The images are recorded at a rate of 10 frames per second such that each frame corresponds to a duration comparable to the duration of the smallest force plateaus. First, we obtain the binary formats of the images processed using the open source Fiji software [1], Fig. 1*C*. The center of the cells are then tracked to extract the local displacement field shown in Fig. 1*D*. Using a coarse-graining technique [2] based on mass conservation, we obtain the coarse-grained displacement field $u_x(x, y)$ and $u_y(x, y)$ as well as the damage field $d(x, y)$ of an equivalent disordered continuum. Fig. 1*E* depicts the field $u_y(x, y)$ during a typical experiment. Taking the gradient of the displacement field, we obtain the strain fields $\epsilon_{xx}(\vec{x}) = \frac{du_x}{dx}$, $\epsilon_{yy}(\vec{x}) = \frac{du_y}{dy}$ and $\epsilon_{xy}(\vec{x}) = \frac{1}{2}\left(\frac{du_x}{dy} + \frac{du_x}{dy}\right)$. The Poisson ratio ν is obtained from a linear fit of $\epsilon_{xx}(\vec{x})$ vs. $\epsilon_{yy}(\vec{x})$ obtained over time and space. To track the damage evolution at the local scale, we define the relative circularity of the cells as our internal damage variable. It turns out that the damage level does not affect the Poisson ratio ($\nu = 0.26$) that remains nearly constant all along the compression test. However, the Young's modulus (E), inferred from the global specimen stiffness $\frac{\sigma_{yy}}{\epsilon_{yy}} = \frac{E}{(1-\nu^2)}$, decays with the average damage level $d_\circ$. In the following, we consider a damage dependent elasticity (elasto-damageability) to describe the constitutive response of the cellular solid. We use the relation $E \sim \mathcal{O}(d_\circ^2)$ inferred from the average elastic modulus of the specimen E and the average damage level $d_\circ$ to determine the field $E_{\text{local}}(\vec{x}, t)$ of local Young's moduli from the damage field $d(\vec{x}, t)$ where $\vec{x} \to (x, y)$. The field of elastic energy stored in the specimen per unit volume is finally

obtained from the relation,

$$E_{\rm el}^{\rm local}(\vec{x},t) = \frac{E_{\rm local}(\vec{x},t)}{2(1-\nu^2)}\left[\epsilon_{\rm xx}^2(\vec{x},t) + \epsilon_{\rm yy}^2(\vec{x},t) + 2\,\nu\epsilon_{\rm xx}(\vec{x},t)\epsilon_{\rm yy}(\vec{x},t) + 2(1-\nu)\epsilon_{\rm xy}^2(\vec{x},t)\right]. \quad (5)$$

$\epsilon_{\rm xx}(\vec{x},t), \epsilon_{\rm yy}(\vec{x},t)$ and $\epsilon_{\rm xy}(\vec{x},t)$ are the local values of normal strains perpendicular and parallel to the direction of loading and shear strains, respectively. At the macroscopic scale, the damage cascades are evidenced from load drops at near constant displacements. At the local scale, they manifest as a local decrease in stored elastic energy of the damaging element. In practice, we consider the material elements for which the elastic energy decreases as damaging elements and compute the local increment of dissipation energy as $\delta E_{\rm d}^{\rm local}(\vec{x}) = -\delta E_{\rm el}^{\rm local}(\vec{x})$. The evolution of the different terms contributing significantly to the total energy of the isolated system composed of the specimen and the loading machine, namely the input work, the elastic energy and the dissipated energy as computed from the global analysis is given in Fig. 1*F*. Our measurement of the total elastic energy from the local strains and elastic moduli are shown to be in good agreement with this global analysis. As damage is accompanied by a decrease in local elastic energy, we obtain the volumteric rate of dissipated energy as

$$\rho(\vec{x},t_i) = b[E_{\rm el}^{\rm local}(\vec{x},t_i) - E_{\rm el}^{\rm local}(\vec{x},t_{i+1})]. \quad (6)$$

where b is the specimen thickness and the time steps t_i correspond to the displacements $\Delta(t_i) \in [\Delta_{\rm ini}, \Delta_{\rm end}]$. Combining all the increments of dissipated energy belonging to the same damage cascade provides the field $\rho(\vec{x}) = \sum_i \rho(\vec{x},t_i)$ of energy dissipated during a given precursor. At the specimen level, we obtain the precursor size byintegration over the whole specimen

$$S_{\rm local} = \iint \rho(x,y)\,{\rm d}x{\rm d}y \quad (7)$$

The distribution of $\rho(\vec{x})$ obtained from all cascades follows an exponential decay $P(\rho) \propto {\rm e}^{-\rho/\rho^*}$ with $\rho^* \simeq 0.18$ J/m^2 (Fig. 1*G*). The value of ρ^* is used as a threshold to obtain binary formats of the dissipation density maps $\rho_{\rm th}(\vec{x})$ of precursors (inset of Fig. 2*A* in the main article).

Spatial extent of the precursors

To determine the spatial extent ξ of the precursors, we compute the 2D auto-correlation of the thresholded dissipation density maps $\rho_{\rm th}(\vec{x})$. The correlation function $C(\delta r) = \langle \rho_{\rm th}(\vec{x}).\rho_{\rm th}(\vec{x}+\delta\vec{x})\rangle_{\vec{x},|\delta\vec{x}|=\delta r} / \langle \rho_{\rm th}(\vec{x})^2\rangle_{\vec{x}}$ is shown in Fig. 1*H* for precursors of different sizes $S_{\rm local}$. The function decreases faster for smaller avalanche size, pointing out a smaller spatial extent. The correlation function can be fitted by an exponential decay $C(\delta r) \propto {\rm e}^{-\delta r/\xi}$, defining the correlation length ξ. This quantity is plotted as a function of the precursors' size and duration in Fig. 2 *C* and *D* of the main article.

Determination of field of the damage resistance

Retrospective determination from the local damage driving force

One of the most appealing feature of our experiments is the full-field measurement of the damage field and its evolution over time. This can be harnessed to access the field of local damage resistance $Y_{\rm c}(\vec{x})$, a quantity that has been hardly measured in the literature, even at the specimen scale. The proposed methodology consists in using the energy based damage criterion

$$\begin{cases} Y[\vec{x},d(\vec{x},t)] & < Y_c[\vec{x},d(\vec{x},t)] \quad \Rightarrow \quad \delta d(\vec{x},t) = 0 \\ Y[\vec{x},d(\vec{x},t)] & = Y_c[\vec{x},d(\vec{x},t)] \quad \Rightarrow \quad \delta d(\vec{x},t) > 0 \end{cases} \quad (8)$$

that, as shown in the following, provides retrospectively the local value of the damage resistance $Y_c[\vec{x},d(\vec{x},t)]$ each time a damage event takes place. First, we compute the field of damage driving force by differentiating Eq. 5 with respect to the damage parameter

$$Y(\vec{x},t) = -\frac{E'_{\rm local}(\vec{x},t)}{2(1-\nu^2)}\left[\epsilon_{xx}^2(\vec{\rm x},t) + \epsilon_{yy}^2(\vec{\rm x},t) + 2\,\nu\epsilon_{xx}(\vec{\rm x},t)\epsilon_{yy}(\vec{\rm x},t) + 2(1-\nu)\epsilon_{xy}^2(\vec{\rm x},t)\right]. \quad (9)$$

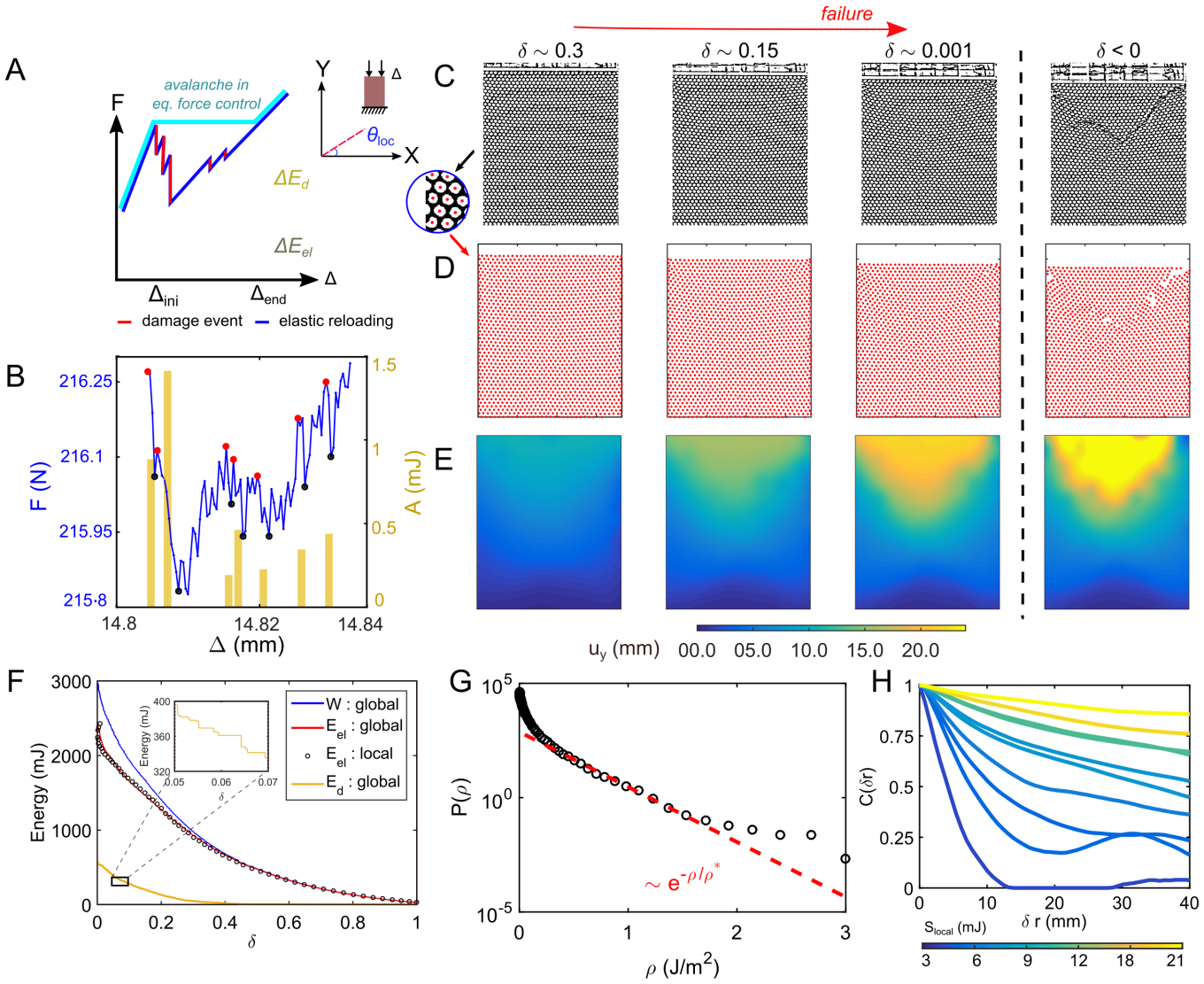

FIG. 1. (A) Schematic of a damage precursor (or avalanche) in an equivalent force control scenario during the compression experiment in displacement control. A schematic representation of the localization angle $\theta_{\rm loc}$. (B) Global analysis of a precursor as measured in our experiments: The damage events constituting the avalanche are revealed by sudden load drops, identified by the red and black circles, denoting the beginning and the end of the event, respectively. The vertical bars provide the size A of the damage event that is defined from the energy dissipated during the event. (C) Binary format of the snapshots of the specimen taken at different distances from localization. (D) The images are post-treated to identify the position of the cell centers that are tracked during the experiment. (E) The displacement of the cell centers with respect to their initial position are coarse-grained to compute the displacement field $u_y(\vec{x})$ at various distances to localization. (F) Evolution of the different energies during the experiment as obtained from our global and local analyses. The work W of the loading machine is converted into elastic energy $E_{\rm el}$ (computed both at the local and global scale) and dissipated energy $E_{\rm d}$. The inset highlights the intermittent evolution of the dissipated energy, a feature reminiscent of the avalanche dynamics of the damage field. (G) Distribution of increments ρ of local dissipation energy density observed during an avalanche – the distribution is computed here from the increments extracted from all the avalanches of a single experiment. It follows an exponential decay $P(\rho) \propto {\rm e}^{-\rho/\rho^\star}$, where the exponential cut-off $\rho^\star \simeq 0.18$ J/m^2 is used to threshold the dissipation energy density maps of single avalanches. (H) Auto-correlation functions $C(\delta r)$ of the thresholded maps of dissipation energy density ρ_{th} of 10 precursors of different sizes. The spatial extent ξ of the precursors is obtained from the fit of the correlation function by an exponential decay $C(\delta r) \propto -{\rm e}^{\delta r/\xi}$. Note that larger precursors have smaller slopes and hence larger spatial extent.

where the derivative to the local elastic modulus $E'_{\rm local} \simeq \frac{dE}{dd_\circ}(d(\vec{x},t))$. Here, we assume that the variations of the average macroscopic elastic modulus with the average damage level $d_\circ$ hold at the local scale too. As schematically illustrated in Fig. 2*A*, the value of the local damage driving force $Y(\vec{x},t)$ is assigned to the damage resistance $Y_{\rm c}(\vec{x},d(\vec{x},t))$ each time a damage event takes place. The damage driving force $Y(\vec{x},t_i)$ at the onset of damage growth t_i is also assigned to the damage resistance $Y_{\rm c}(\vec{x},d(\vec{x},\underset{\sim}{t})) = Y(\vec{x},t_i)$ during the whole sequence of elastic reloading preceding t_i, i.e. for $\underset{\sim}{t} \in [t_{i-k},t_{i-1}...t_i]$ where t_{i-k} is the time at which the previous damage event in the same material element $\vec{x}$ took place. Now considering the average damage resistance $Y_{\rm c\circ}(d_\circ) = \langle Y_{\rm c}(\vec{x},d(\vec{x},t))\rangle_{d(\vec{x},t)=d_\circ}$ at some given damage level $d_\circ$, we see in Fig. 2*B* that, after an initial transient regime during which damage evolution is dominated by randomly distributed small localized events, $Y_{\rm c\circ}(d_\circ)$ *increases* with damage. This hardening can be described by a linear relation $Y_{\rm c\circ}(d_\circ) = Y_{\rm c}^\circ(1+\eta\, d_\circ)$ where $Y_{\rm c}^\circ \simeq 1.4$ kJ/m^3 and $\eta \simeq 44$.

Alternative methodology: determination from the accumulated dissipated energy

As an alternative to the above retrospective determination of Y_c at the local scale, the average value of damage resistance can be estimated from the variation of accumulated dissipated energy using

$$Y_{c\circ}(d_\circ) = \frac{1}{V_\circ}\frac{dE_d}{dd_\circ} \tag{10}$$

where $V_\circ$ is the initial volume of the cellular solid and E_d is the accumulated dissipated energy obtained from the global balance of energy (see inset of Fig. 2*C*). Assuming a linear variation $Y_{c\circ} \propto \eta d_\circ$, the accumulated dissipated energy is fitted by a quadratic function providing $Y_c^\circ = 1.1$kJ/m^3 and $\eta \simeq 45$, both values that are close to the one inferred from the previous method. Using this linear relation, we then determine the field of damage resistance $Y_c(\vec{x},t) = Y_{c\circ}(d(\vec{x},t))$ from the damage field. The energy dissipated at each time step is then computed as $\rho(\vec{x},t_i) = \max(Y_c(\vec{x},t_i)\delta d(\vec{x},t_i),0)$, where $\delta d(\vec{x},t_i)$ is the incremental damage growth in $\vec{x}$. The dissipated energy density $\rho(\vec{x})$ during one precursor and the precursor size S_{local} follow from (7). A comparison with the first method is presented in Fig. 2*D* that shows a good agreement. The maps of local dissipated energy density of a typical cascade as obtained from the two approaches are compared in Fig. 2*E*. The discrepancies in the maps of the dissipation energy density are localized at the periphery of the specimen where the rather large damage may be attributed to frictional effects with the walls. Thus, we observe a good agreement between both methods, thus validating the assumption of local energy balance made previously.

Theoretical modeling of the evolution of the damage field

We now detail the damage model used to describe our experiments. It intends to account for the co-action of material disorder and long-range elastic interactions in the aftermath of a damage event, in the spirit of the physics-based non-local damage models proposed in Berthier *et al.* [3] and Dansereau *et al.* [4]. In particular, we provide the redistribution kernel characterizing the long-range interactions derived here for the particular case of a 2D specimen compressed between two fixed lateral walls. The first step, detailed in sections and for force and displacement imposed conditions, respectively consists in calculating the distribution of damage driving force resulting from a heterogeneous distribution of damage (see Eqs. (19) and (25) that we write in a generic form valid for both loading conditions in (27)). We then extend our calculations to the case of a monotonically increasing loading amplitude in section . In section we derive the damage evolution equation from the damage criterion of (8). We then explain in section how the evolution equation of the damage field belongs to the theoretical framework of driven disordered elastic interfaces. The stability of the damage spreading process is studied in section . The localization threshold is shown to coincide with peak load. Lastly, we show in section that the rate of damage growth diverges on approaching localization.

We start by considering that the level of damage in each material element located in $\vec{x}$ is $d(\vec{x}) \geq 0$, where $d = 0$ corresponds to the intact initial material. The level of damage is assumed to affect the elastic modulus $E[d(\vec{x})]$ of the cellular solid. Its Poisson's ratio ν is assumed to be independent of the damage level, as supported by our experimental observations (Sec. S1C). The constitutive behavior of the cellular solid is then the one of an elasto-damageable solid under plane stress conditions

$$\boldsymbol{\epsilon} = \frac{(1+\nu)\boldsymbol{\sigma} - \nu{\rm Tr}(\boldsymbol{\sigma})}{E}. \tag{11}$$

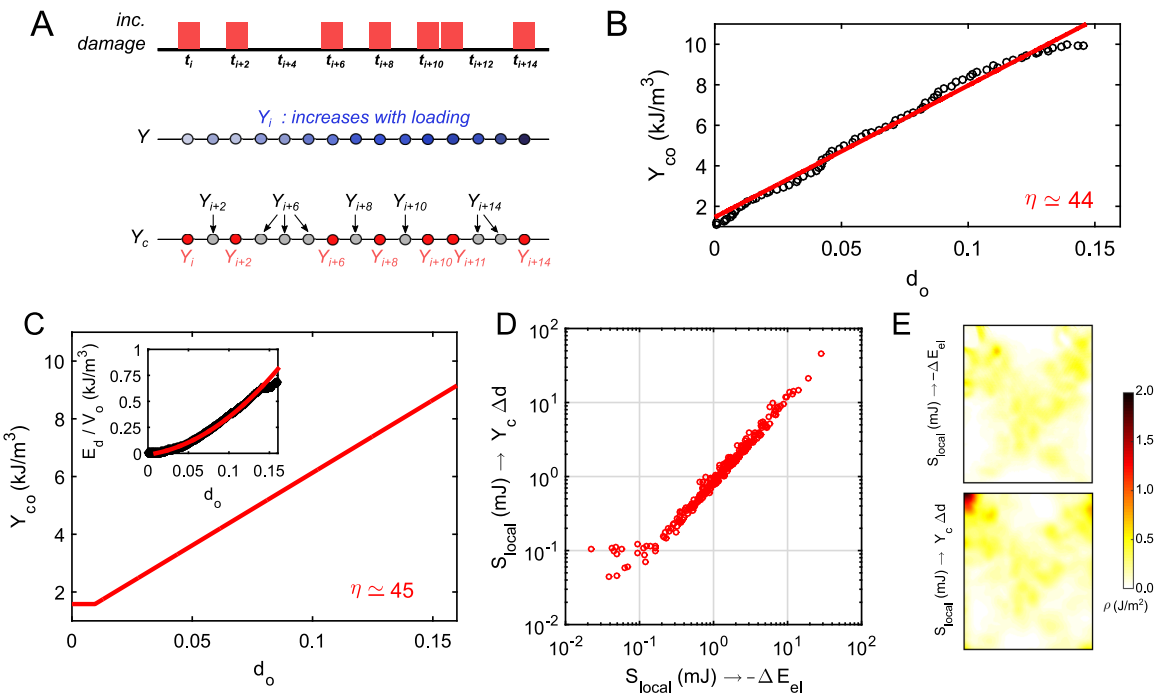

FIG. 2. (A) Schematic of the retrospective assignment procedure used to determine the local damage resistance $Y_c[\vec{x}, d(\vec{x},t)]$ from the field of damage driving force $Y[\vec{x}, d(\vec{x},t), t]$. (B) Variations of the average damage resistance Y_{co} with respect to the damage level d_o. The increase of the damage resistance can be described by a linear hardening $Y_{co}(d_o) = Y_c^\circ(1+\eta\, d_o)$ with a hardening coefficient $\eta \simeq 44$. (C) Variations of the average damage resistance Y_{co} with the average damage level d_o inferred from the variations with respect to $d-\circ$ of the accumulated dissipated energy at the specimen level that can be described (see inset) by a quadratic function (in red). (D) Comparison of the precursor size $S_{\rm local}$ obtained our two independent methods: from the variations of elastic energy in the abscissa and from the local increase of the damage variable and the damage resistance $Y_{co}(d_o)$ in the ordinates. (E) Dissipated energy density maps of a typical precursor as obtained from the two methods.

Due to the lateral confinement ($\epsilon_{xx} = 0$), the in-plane stress components follow: $\sigma_{yy} = \epsilon_{yy}E/(1-\nu^2)$ along the loading direction and $\sigma_{xx} = \nu\sigma_{yy}$ along the lateral direction. In absence of out-of-plane stress ($\sigma_{zz} = 0$), Hooke's law predicts $\epsilon_{zz} = -\epsilon_{yy}\nu/(1-\nu)$. The elastic energy per unit volume of the material, $w(\boldsymbol{\epsilon}, \boldsymbol{\sigma}) = (1/2)\ \boldsymbol{\epsilon}\colon\boldsymbol{\sigma}$, can then be expressed as

$$w(\boldsymbol{\epsilon}, \boldsymbol{\sigma}) = \frac{(1+\nu)\mathrm{Tr}(\boldsymbol{\sigma}^2) - \nu\mathrm{Tr}(\boldsymbol{\sigma})^2}{2E} \tag{12}$$

Damage driving force under force control conditions

For a homogeneous damage level $d_\circ$, the elastic energy release rate that drives damage growth follows

$$Y(d_\circ, \boldsymbol{\sigma}) = \left.\frac{\partial w}{\partial d_\circ}\right|_{\boldsymbol{\sigma}} = \frac{\overline{\mu}'(d_\circ)\mathrm{Tr}(\boldsymbol{\sigma}^2)}{4} + \frac{\nu E'(d_\circ)\mathrm{Tr}(\boldsymbol{\sigma})^2}{2E(d_\circ)^2} \tag{13}$$

where $\mu = E/2(1+\nu)$ is the Lamé constant and $\overline{\mu} = 1/\mu$. The prime denotes the derivative with respect to the damage variable $d_\circ$. To examine the effect of material disorder on the damage field and in particular on the stress redistributions following individual damage events, we introduce weak variations in the damage field $d(\vec{x}) = d_\circ + \delta d(\vec{x})$ where $d_\circ$ is the average damage level and $\delta d(\vec{x}) \ll d_\circ$ are its perturbations. The heterogeneities in the damage field result from the spatial variations of the elastic modulus. Consequently, the stress field is heterogeneous and writes as $\boldsymbol{\sigma}(\vec{x}) = \boldsymbol{\sigma}_\circ + \delta\boldsymbol{\sigma}(\vec{x})$ where

$$\boldsymbol{\sigma}_\circ = \sigma_{\rm ext}\begin{bmatrix}\nu & 0 & 0\\ 0 & 1 & 0\\ 0 & 0 & 0\end{bmatrix} \text{ and } \delta\boldsymbol{\sigma}(\vec{x}) = \begin{bmatrix}\delta\sigma_{xx}(\vec{x}) & \delta\sigma_{xy}(\vec{x}) & 0\\ \delta\sigma_{yx}(\vec{x}) & \delta\sigma_{yy}(\vec{x}) & 0\\ 0 & 0 & 0\end{bmatrix}. \tag{14}$$

Here, $\sigma_{\text{ext}} = F/bL$ is the average stress imposed by the loading machine to the upper surface bL of the specimen. As a consequence, the damage driving force provided in (13) is also heterogeneous and can be decomposed as $Y[d(\vec{x})] = Y_\circ(d_\circ) + \delta Y[d(\vec{x})]$ where

$$\left\{\begin{array}{ll} Y_\circ(d_\circ, \boldsymbol{\sigma}_\circ) & = \frac{\overline{\mu}'(d_\circ)\text{Tr}(\boldsymbol{\sigma}_\circ^2)}{4} + \frac{\nu E'(d_\circ)\text{Tr}(\boldsymbol{\sigma}_\circ)^2}{2E(d_\circ)^2} \\ \delta Y[d(\vec{x}), \boldsymbol{\sigma}_\circ] & = \left[\frac{\overline{\mu}''(d_\circ)\text{Tr}(\boldsymbol{\sigma}_\circ^2)}{4} - \frac{\nu\text{Tr}(\boldsymbol{\sigma}_\circ)^2}{2}\left(\frac{2E'(d_\circ)^2}{E(d_\circ)^3} - \frac{E''(d_\circ)}{E(d_\circ)^2}\right)\right]\delta d(\vec{x}) + \left[\frac{\overline{\mu}'(d_\circ)\text{Tr}(\boldsymbol{\sigma}_\circ\delta\boldsymbol{\sigma}(\vec{x}))}{2} + \frac{\nu E'(d_\circ)\text{Tr}(\boldsymbol{\sigma}_\circ)\text{Tr}(\delta\boldsymbol{\sigma}(\vec{x}))}{E(d_\circ)^2}\right]. \end{array}\right. \tag{15}$$

The first term in the expression of $\delta Y[d(\vec{x})]$ is a local term, namely its value in $\vec{x}$ depends only on the damage level in $\vec{x}$. It can be obtained by considering a homogeneous damage level $d_\circ$ and varying $Y[d_\circ = d(\vec{x})]$ with respect to it as follows

$$\left.\frac{\partial Y_\circ}{\partial d_\circ}\right|_{\sigma_\circ} = \frac{(1-\nu^2)}{2}\sigma_{ext}^2\left[\frac{2E'(d_\circ)^2}{E(d_\circ)^3} - \frac{E''(d_\circ)}{E(d_\circ)^2}\right]. \tag{16}$$

To calculate the non-local contributions to $\delta Y[d(\vec{x})]$ (i.e., the second term in (15)) we first need to evaluate the stress perturbations $\delta\boldsymbol{\sigma}(\vec{x})$ emerging from the spatial variations of elastic modulus, as performed in Dansereau *et al.* [4]. We then use a perturbative approach in Fourier space and such calculations that gives

$$\delta\tilde{\boldsymbol{\sigma}}(q_x, q_y) = \frac{\overline{\mu}'(d_\circ)}{\overline{\mu}(d_\circ)}\left(\mathbf{O}\cdot\boldsymbol{\sigma}_\circ\cdot\mathbf{O} - \nu\left[(1-\mathbf{O}) : \boldsymbol{\sigma}_\circ\right]\mathbf{O}\right)\delta\tilde{d}(q_x, q_y), \tag{17}$$

where $\mathbf{O}$ stands for the Oseen tensor, $\mathbf{O} = 1 - \mathbf{Q}$ with the tensor $\mathbf{Q_{ij}} = q_i q_j/|\vec{q}|^2$. $\delta\tilde{\boldsymbol{\sigma}}(q_x, q_y)$ and $\delta\tilde{d}(q_x, q_y)$ are the 2D Fourier transform of the stress field perturbations and the damage field perturbations, respectively. Substituting (17) into (15), we obtain the non-local contributions to the damage driving force that writes as $\tilde{\psi}\delta\tilde{d}$ in Fourier space, that defines the interaction kernel $\tilde{\psi}(q_x, q_y)$. In real space and in polar coordinates, it writes as $\psi(r, \theta) \sim g(\theta)/r^2$, where r is the distance from the damage event at the origin of the stress redistribution and $g(\theta)$ is an angular function with $\theta = \arctan(y/x)$. As expected, the elastic interactions decay as a power law of the distance r, resulting in long-range interactions between material elements during damage spreading. The interaction kernel, derived here for the case of uni-axial compression with lateral confinement follows

$$\psi(d_\circ) = \left[\frac{E'(d_\circ)^2}{E(d_\circ)^3}\right](1-\nu^2)\sigma_{ext}^2\left[\frac{x^4 - 3y^4 + 6x^2y^2}{4\pi(x^2+y^2)^3}\right] \rightarrow ||\psi||\left[\frac{\cos^4\theta - 3\sin^4\theta + 6\cos^2\theta\sin^2\theta}{4\pi r^6}\right] \tag{18}$$

in cartesian coordinates. The pre-factor $||\psi(d_\circ)|| = \frac{E'(d_\circ)^2}{E(d_\circ)^3}(1-\nu^2)\sigma_{\text{ext}}^2$ is independent of $\vec{x}$. In Fourier space, the interaction kernel follows $\tilde{\psi}(\vec{q}) \sim \frac{q_x}{||\vec{q}||} \sim -cos^4(\omega)$ where $\omega = \arctan(\frac{q_x}{q_y})$. We finally obtain the spatial distribution of damage driving force

$$Y[d(\vec{x}), \boldsymbol{\sigma}_\circ] = Y(d_\circ, \boldsymbol{\sigma}_\circ) + \left.\frac{\partial Y_\circ}{\partial d_\circ}\right|_{\boldsymbol{\sigma}_\circ}\delta d(\vec{x}) + \psi(d_\circ) * \delta d(\vec{x}). \tag{19}$$

Interestingly, the kernel $\psi(d_\circ)$ that describes here the distribution of damage driving force in a heterogeneously damaged specimen can also be interpreted as describing the driving force redistribution following an individual damage event. Considering the damage perturbations $\delta d(\vec{x}) = \delta(\vec{x} - \vec{x_0})\delta d_\circ$ corresponding to an individual event taking place in $\vec{x_0}$ where $\delta(u)$ is the Dirac function and $\delta d_\circ$ the damage event amplitude, we obtain the spatial distribution of incremental driving force $\delta Y(\vec{x}) = \delta d_\circ\psi(\vec{x} - \vec{x_0})$ resulting from the damage event. It turns out that the material regions located next to $\vec{x}_\circ$ perpendicularly to the loading axis are reloaded while the material regions located below and above the damaged element are screened as shown in Fig.3(A).

Damage driving force under displacement control conditions

The driving force for damage growth computed in (13) for a homogeneous distribution of damage level $d_\circ$ is now expressed as a function of the strain field $\boldsymbol{\epsilon}$

$$Y(d_\circ, \boldsymbol{\epsilon}) = -\mu'(d_\circ)\text{Tr}(\boldsymbol{\epsilon}^2) - \frac{\lambda'(d_\circ)\text{Tr}(\boldsymbol{\epsilon})^2}{2}, \tag{20}$$

where $\mu = E/2(1+\nu)$ and $\lambda = E\nu/(1-2\nu)(1+\nu)$ are the Lamé constants. It is important to note that the expression of Y does not depend on the type of loading conditions, i.e., Eqs. (20) and (13) are equivalent. In presence of weak variations of the damage field $d(\vec{x}) = d_\circ + \delta d(\vec{x})$, the strain field writes as the sum of two contributions $\boldsymbol{\epsilon} = \boldsymbol{\epsilon}_\circ + \delta\boldsymbol{\epsilon}$ where

$$\boldsymbol{\epsilon}_\circ = \epsilon_{ext}\begin{bmatrix} 0 & 0 & 0 \\ 0 & 1 & 0 \\ 0 & 0 & -\frac{\nu}{1-\nu} \end{bmatrix} \text{ and } \delta\boldsymbol{\epsilon}(\vec{x}) = \begin{bmatrix} \delta\epsilon_{xx}(\vec{x}) & \delta\epsilon_{xy}(\vec{x}) & 0 \\ \delta\epsilon_{yx}(\vec{x}) & \delta\epsilon_{yy}(\vec{x}) & 0 \\ 0 & 0 & 0 \end{bmatrix}. \tag{21}$$

The field of damage driving force, $Y[d(\vec{x}), \boldsymbol{\epsilon}_\circ] = Y_\circ(d_\circ, \boldsymbol{\epsilon}_\circ) + \delta Y[d(\vec{x}), \boldsymbol{\epsilon}_\circ]$, including its perturbations $\delta Y[d(\vec{x}), \boldsymbol{\epsilon}_\circ]$ follows

$$\begin{cases} Y_\circ(d_\circ, \boldsymbol{\epsilon}_\circ) & = -\mu'(d_\circ)\mathrm{Tr}(\boldsymbol{\epsilon}_\circ^2) - \frac{\lambda'(d_\circ)\mathrm{Tr}(\boldsymbol{\epsilon}_\circ)^2}{2}, \\ \delta Y[d(\vec{x}), \boldsymbol{\epsilon}_\circ] & = -\left[\mu''(d_\circ)\mathrm{Tr}(\boldsymbol{\epsilon}_\circ^2) + \frac{\lambda''(d_\circ)\mathrm{Tr}(\boldsymbol{\epsilon}_\circ)^2}{2}\right]\delta d(\vec{x}) - \left[2\mu'(d_\circ)\mathrm{Tr}(\boldsymbol{\epsilon}_\circ\delta\boldsymbol{\epsilon}(\vec{x})) + \lambda'(d_\circ)E'\mathrm{Tr}(\boldsymbol{\epsilon}_\circ)\mathrm{Tr}(\delta\boldsymbol{\epsilon}(\vec{x}))\right]. \end{cases} \tag{22}$$

$\delta\boldsymbol{\epsilon}(\vec{x})$ follows from (11)

$$\delta\boldsymbol{\epsilon}(\vec{x}) = \left[\frac{(1+\nu)\delta\boldsymbol{\sigma}(\vec{x}) - \nu\mathrm{Tr}(\delta\boldsymbol{\sigma}(\vec{x}))}{E(d_\circ)}\right] - \left[\frac{E'(d_\circ)}{E(d_\circ)^2}\right]\left[(1+\nu)\boldsymbol{\sigma}_\circ - \nu\mathrm{Tr}(\boldsymbol{\sigma}_\circ)\right]. \tag{23}$$

The first term in bracket in (22) provides the local contribution to the driving force perturbations

$$\left.\frac{\partial Y_\circ}{\partial d_\circ}\right|_{\epsilon_\circ} = -\left[\frac{E''(d_\circ)}{E(d_\circ)^2}\right]\frac{(1-\nu^2)}{2}\sigma_{\text{ext}}^2. \tag{24}$$

Using (23), the second term in brackets in (22) simplifies as $\left[\frac{2E'(d_\circ)^2}{E(d_\circ)^3}\right]\frac{(1-\nu^2)}{2}\sigma_{\text{ext}}^2\delta d(\vec{x}) + \psi(d_\circ) * \delta d(\vec{x})$ where $\psi(d_\circ)$ is the interaction kernel given in (12). Thus, the field of damage driving force under displacement control conditions writes as

$$Y[d(\vec{x}), \boldsymbol{\epsilon}_\circ] = Y(d_\circ, \boldsymbol{\epsilon}_\circ) + \left.\frac{\partial Y_\circ}{\partial d_\circ}\right|_{\epsilon_\circ}\delta d(\vec{x}) + \left(\left[\frac{2E'(d_\circ)^2}{E(d_\circ)^3}\right]\frac{(1-\nu^2)}{2}\sigma_{\text{ext}}^2\right)\delta d(\vec{x}) + \psi(d_\circ) * \delta d(\vec{x}). \tag{25}$$

Comparing (25) with (19) and noticing that the spatial distribution of damage driving force is independent of the type of loading conditions, we obtain

$$\begin{aligned} \left.\frac{\partial Y_\circ}{\partial d_\circ}\right|_{\boldsymbol{\sigma}_\circ} &= \left.\frac{\partial Y_\circ}{\partial d_\circ}\right|_{\boldsymbol{\epsilon}_\circ} + \left[\frac{2E'(d_\circ)^2}{E(d_\circ)^3}\right]\frac{(1-\nu^2)}{2}\sigma_{\text{ext}}^2, \\ &= \left.\frac{\partial Y_\circ}{\partial d_\circ}\right|_{\boldsymbol{\epsilon}_\circ} + ||\psi(d_\circ)||. \end{aligned} \tag{26}$$

Finally we can generalize the damage driving force corresponding to a perturbed damage field $d(\vec{x}) = d_\circ + \delta d(\vec{x})$ using

$$Y[d(\vec{x})] = Y_\circ(d_\circ) + \Psi(d_\circ) * \delta d(\vec{x}), \tag{27}$$

where the generalized interaction kernel follows $\Psi(d_\circ) = \left.\frac{\partial Y_\circ}{\partial d_\circ}\right|_{\sigma_\circ}\delta(\vec{x}) + \psi(d_\circ)$. The first term provides the local contribution to the damage driving force while the second term corresponds to the non-local part controlled by the interaction kernel ψ.

Damage evolution under increasing loading amplitude

We now examine the evolution of the damage field $d(\vec{x}, t)$ in response to an external driving $X_\circ(t)$ (which can be either force or displacement) that increases linearly with time: $X_\circ = X_\circ(0) + v_{\text{ext}}t$. The damage field can be expressed as $d(\vec{x}, t) = d_\circ(0) + \Delta d(\vec{x}, t)$, where the incremental damage field $\Delta d(\vec{x}, t) \ll d_\circ(0)$. Therefore, the reference (homogeneous) damage level corresponding to the driving $X_\circ(t)$ is $d_\circ(t) = d_\circ(0) + \langle\Delta d\rangle_{\vec{x}}(t)$ and the corresponding

damage field perturbations writes as $\delta d(\vec{x},t) = \Delta d(\vec{x},t) - \langle \Delta d \rangle_{\vec{x}}$. We now use the previous result of (27) to obtain the damage driving force

$$Y[d(\vec{x},t), X_\circ(t)] = Y_\circ[d_\circ(t), X_\circ(t)] + \Psi(d_\circ) * [\Delta d(\vec{x},t) - \langle \Delta d \rangle_{\vec{x}}]\,. \tag{28}$$

Note that this linearization remains valid over a short period of time $t \ll X_\circ / v_{\text{ext}}$ where v_{ext} is the velocity of the external driving imposed by loading machine. By expanding the first term and using the expression of the kernel Ψ, one obtains

$$\begin{aligned} Y[d(\vec{x},t),t] = Y[d_\circ(0), X_\circ(0)] + \left.\frac{\partial Y_\circ}{\partial X_\circ}\right|_{d_\circ(0)} v_{\text{ext}} t + \left.\frac{\partial Y_\circ}{\partial d_\circ}\right|_{X_\circ(0)} \langle \Delta d \rangle_{\vec{x}} \quad + \\ \left.\frac{\partial Y_\circ}{\partial d_\circ}\right|_{\boldsymbol{\sigma}_\circ(0)} [\Delta d(\vec{x},t) - \langle \Delta d \rangle_{\vec{x}}] + \psi[d_\circ(0)] * [\Delta d(\vec{x},t) - \langle \Delta d \rangle_{\vec{x}}] \end{aligned} \tag{29}$$

where only first order terms proportional to Δd have been kept. For the force control case ($X_\circ \to \boldsymbol{\sigma}_\circ$), the damage driving force is given by

$$Y[d(\vec{x},t),t] = Y[d_\circ(0), \boldsymbol{\sigma}_\circ(0)] + \left.\frac{\partial Y_\circ}{\partial \sigma_\circ}\right|_{d_\circ(0)} v_{\text{ext}} t + \left.\frac{\partial Y_\circ}{\partial d_\circ}\right|_{\boldsymbol{\sigma}_\circ(\mathbf{0})} \Delta d(\vec{x},t) + \psi[d_\circ(0)] * [\Delta d(\vec{x},t) - \langle \Delta d \rangle_{\vec{x}}]\,. \tag{30}$$

Similarly, under displacement control conditions ($X_\circ \to \boldsymbol{\epsilon}_\circ$) the damage driving force writes as

$$Y[d(\vec{x},t),t] = Y[d_\circ(0), \boldsymbol{\epsilon}_\circ(0)] + \left.\frac{\partial Y_\circ}{\partial \epsilon_\circ}\right|_{d_\circ(0)} v_{\text{ext}} t + \left.\frac{\partial Y_\circ}{\partial d_\circ}\right|_{\boldsymbol{\sigma}_\circ(0)} \Delta d(\vec{x},t) + \psi[d_\circ(0)] * [\Delta d(\vec{x},t) - \langle \Delta d \rangle_{\vec{x}}] - ||\psi[d_\circ(0)]|| \langle \Delta d \rangle_{\vec{x}}. \tag{31}$$

where the (26), $\left.\frac{\partial Y_\circ}{\partial d_\circ}\right|_{\boldsymbol{\epsilon}_\circ(0)} = \left.\frac{\partial Y_\circ}{\partial d_\circ}\right|_{\boldsymbol{\sigma}_\circ(0)} - ||\psi[d_\circ(0)]||$ has been used. The damage driving force under force and displacement control conditions are thus similar, up to the last term in (31). This term acts as a mean-field restoring force. Its effect on the stability of the damage growth process is discussed in the following.

Generalized damage driving force

We now consider the resistance to damage growth $Y_c[d(\vec{x},t)]$. Its linearized expression follows

$$Y_c[d(\vec{x},t)] = Y_c^\circ[d_\circ(0)] + \left.\frac{dY_{c\circ}}{dd_\circ}\right|_{d_\circ(0)} \Delta d(\vec{x},t) + y_c[\vec{x}, d(\vec{x},t)] \tag{32}$$

where $\frac{dY_{c\circ}}{dd_\circ} = Y_c^\circ \eta$ with Y_c° the damage resistance of the intact material, η the hardening parameter and $y_c[\vec{x}, d(\vec{x},t)] = Y_c[d(\vec{x},t)] - Y_{c\circ}(d_\circ)$, the heterogeneous contribution to the field of damage resistance. It is practical to introduce the generalized damage driving force

$$\mathcal{F}[d(\vec{x},t),t] = Y[d(\vec{x},t),t] - Y_c[d(\vec{x},t)]. \tag{33}$$

In particular, under force control conditions, the expression of the generalized driving force can be written, following (30), as

$$\mathcal{F}[d(\vec{x},t),t] = \left.\frac{\partial Y_\circ}{\partial \boldsymbol{\sigma}_\circ}\right|_{d_\circ(0)} v_{\text{ext}} t + \left.\frac{\partial (Y_\circ - Y_{c\circ})}{\partial d_\circ}\right|_{\boldsymbol{\sigma}_\circ(0)} \Delta d(\vec{x},t) + \psi[d_\circ(0)] * [\Delta d(\vec{x},t) - \langle \Delta d \rangle_{\vec{x}}] - y_c[\vec{x}, d(\vec{x},t)]. \tag{34}$$

The generalized driving force under displacement control conditions follows

$$\mathcal{F}[d(\vec{x},t),t] = \left.\frac{\partial Y_\circ}{\partial \boldsymbol{\epsilon}_\circ}\right|_{d_\circ(0)} v_{\text{ext}} t + \left.\frac{\partial (Y_\circ - Y_{c\circ})}{\partial d_\circ}\right|_{\boldsymbol{\sigma}_\circ(0)} \Delta d(\vec{x},t) + \psi[d_\circ(0)] * [\Delta d(\vec{x},t) - \langle \Delta d \rangle_{\vec{x}}] - y_c[\vec{x}, d(\vec{x},t)] - ||\psi[d_\circ(0)]|| \langle \Delta d \rangle_{\vec{x}} \tag{35}$$

Analogy to driven disordered elastic interfaces

The framework of driven disordered elastic interfaces describes the intermittent response of an elastic manifold to a continuous external drive as it propagates through a disordered field of resistance. Following a local depinning event, the co-action of disorder and elasticity may generate a cascade of depinning events. This phenomenon yields robust scaling laws relating the characteristic features of the cascades all together - size, duration and spatial extent. Here, we seek to recast the evolution equation of the damage field under force controlled conditions to the one of a driven pseudo-interface. By considering an over-damped dynamics $\dot{\Delta}d \propto \mathcal{F}$, where $\dot{\Delta}d$ is the local damage growth rate, and rearranging the terms of (34), we obtain

$$\dot{\Delta}d(\vec{x},t) \propto \mathcal{K}\left[v_{\mathrm{m}}t - \Delta d(\vec{x},t)\right] + \psi[d_\circ(0)] * \left[\Delta d(\vec{x},t) - \langle \Delta d\rangle_{\vec{x}}\right] - y_c[\vec{x}, d(\vec{x},t)], \tag{36}$$

$$\text{where } \mathcal{K}[\boldsymbol{\sigma}_\circ(0)] = \left.\frac{\partial(Y_{c\circ} - Y_\circ)}{\partial d_\circ}\right|_{\boldsymbol{\sigma}_\circ(0)} \quad \text{and} \quad v_{\mathrm{m}}[\boldsymbol{\sigma}_\circ(0)] = \frac{\partial Y_\circ/\partial \boldsymbol{\sigma}_\circ}{\mathcal{K}[\boldsymbol{\sigma}_\circ(0)]} v_{\mathrm{ext}}. \tag{37}$$

Equation (36) describes a 2D elastic interface driven through a heterogeneous field of damage resistance $y_c[\vec{x}, d(\vec{x},t)]$. The interface is driven at an average speed v_{m} by Hookean springs of stiffness $\mathcal{K}$ connecting the interface to a rigid plate moving at the speed v_{m}, as schematically illustrated in Fig. 3. The competition between the disorder in the field $y_c[\vec{x}, d(\vec{x},t)]$ of damage resistance and the interface elasticity controls the roughness $\delta d(\vec{x},t)$ of the interface. Following each damage event, multiple regions of the interface may move forward as a result of the redistribution of the local driving force along the interface, leading to cascades of damage events. Notably, the disorder $y_c[\vec{x}, d(\vec{x},t)]$ is a function of both the location $\vec{x}$ and the damage field $d(\vec{x},t)$, so it takes the value of damage resistance actually visited by the interface. This leads to the strongly non-linear response of the interface to the smoothly varying drive observed in our experiments. Under displacement control conditions, the damage evolution follows a similar equation

$$\dot{\Delta}d(\vec{x},t) \propto \mathcal{K}\left[v_{\mathrm{m}}t - \Delta d(\vec{x},t)\right] + \psi[d_\circ(0)] * \left[\Delta d(\vec{x},t) - \langle \Delta d\rangle_{\vec{x}}\right] - y_c[\vec{x}, d(\vec{x},t)] - ||\psi[d_\circ(0)]||\langle \Delta d\rangle_{\vec{x}} \tag{38}$$

$$\text{where } \mathcal{K}[\boldsymbol{\sigma}_\circ(0)] = \left.\frac{\partial(Y_{c\circ} - Y_\circ)}{\partial d_\circ}\right|_{\boldsymbol{\sigma}_\circ(0)} \quad \text{and} \quad v_{\mathrm{m}}[\boldsymbol{\epsilon}_\circ(0)] = \frac{\partial Y_\circ/\partial \boldsymbol{\sigma}_\circ}{\mathcal{K} + ||\psi||} v_{\mathrm{ext}} \tag{39}$$

where the relation $\frac{\partial \boldsymbol{\sigma}_\circ}{\partial \boldsymbol{\epsilon}_\circ} = \frac{E}{(1-\nu^2)}\frac{\mathcal{K}}{\mathcal{K}+||\psi||}$ has been used. The comparison of the Eqs. (37) and (38) shows that the mean damage growth rate v_{m} normalized by the loading rate v_{ext} (that provides the speed of the rigid plate pulling on the interface) is slower under displacement control conditions. In addition, an extra term $\sim -\langle \Delta d\rangle_{\vec{x}}$ that contributes to stiffen the interface (and so to stabilize it), applies.

Onset of damage localization

We use our theoretical framework to investigate the stability of the damage growth process. Consider a homogeneous system, i.e., $y_c[\vec{x}, d(\vec{x},t)] = 0$ and a harmonic positive perturbation of the damage field $d(\vec{x}) = d_\circ + \Delta d_\circ(1+\cos(\vec{q_\circ}\cdot\vec{x}))$ of amplitude $\Delta d_\circ$. The corresponding damage driving force $\mathcal{F}$ derived in Eqs. (34) and (35) writes as

$$\begin{aligned}
&\mathcal{F}(\vec{q_\circ}\cdot\vec{x}) = \mathcal{K}(d_\circ)\left[v_{\mathrm{m}}t - \Delta d_\circ\right]\delta(\vec{x}) + \left[\psi(d_\circ) - \mathcal{K}(d_\circ)\delta(\vec{x})\right] * \Delta d_\circ \cos(\vec{q_\circ}\cdot\vec{x}) && \text{under force control conditions,}\\
&\mathcal{F}(\vec{q_\circ}\cdot\vec{x}) = \mathcal{K}(d_\circ)\left[v_{\mathrm{m}}t - \Delta d_\circ\right]\delta(\vec{x}) + \left[\psi(d_\circ) - \mathcal{K}(d_\circ)\delta(\vec{x})\right] * \Delta d_\circ \cos(\vec{q_\circ}\cdot\vec{x}) - ||\psi(d_\circ)||\Delta d_\circ && \text{under displacement control conditions}
\end{aligned} \tag{40}$$

Assuming a homogeneous perturbation $d(\vec{x}) = d_\circ + \Delta d_\circ$, the convolution product vanishes and the stability criterion of the damage evolution reduces to

$$\begin{cases} \mathcal{K} > 0 & \text{under force control conditions,}\\ \mathcal{K} + ||\psi|| \ > 0 & \text{under displacement control conditions.}\end{cases} \tag{41}$$

These conditions provide the homogeneous damage level at which the damage evolution is unstable. Under force control conditions, it corresponds to peak load where $\mathcal{K} = \left.\frac{\partial(Y_\circ - Y_{c\circ})}{\partial d_\circ}\right|_{\boldsymbol{\sigma}_\circ}$ changes sign. Under displacement control, the stability criterion predicts that damage growth is more stable as $\mathcal{K} + ||\psi(d_\circ)|| > \mathcal{K}$. In particular, the stability

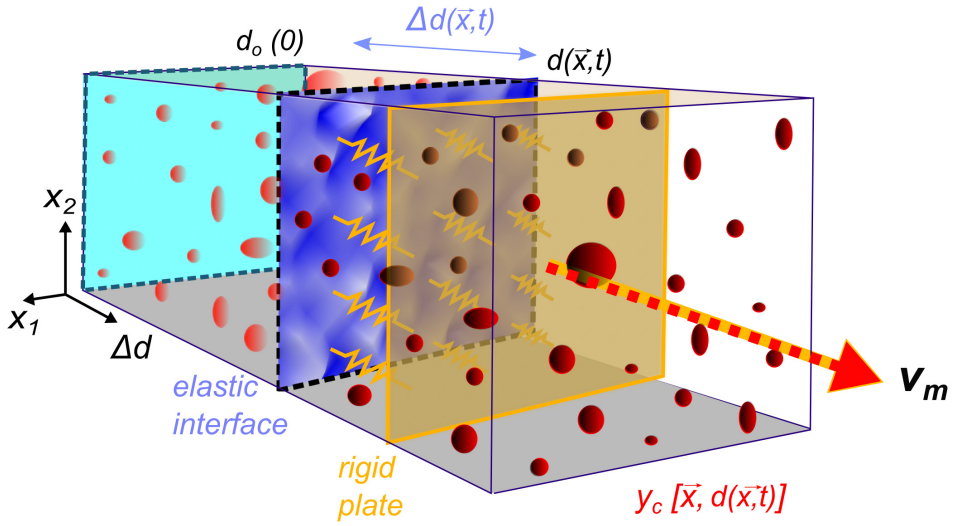

FIG. 3. Schematic representation of the damage level as an elastic interface (in blue) driven through a disordered field of damage resistance $y_c[\vec{x}, d(\vec{x},t)]$. The red blobs are representative of the regions of relatively higher value of damage resistance. The interface is initially flat $d_\circ(0)$. The rigid plate (in yellow) is driven at the speed v_m and pulls on the interface with linear springs of stiffness $\mathcal{K}$. Consequently the interface also moves with an average velocity v_m. The interplay between the disorder and the interface elasticity roughens the interface $d(\vec{x},t)$ at time t and leads to an avalanche-like dynamics as it progresses through the disorder field of damage resistance.

condition is ensured even beyond peak load. Equation (40) also provides the perturbations in damage driving force resulting from periodic perturbations $\Delta d_\circ \cos(\vec{q_\circ} \cdot \vec{x})$ of the damage field. The emergence of the localization band is inferred from the criterion [4].

$$\tilde{\psi}(\vec{q_\circ}, d_\circ) - \mathcal{K}(d_\circ) = 0, \tag{42}$$

Indeed, (42) ensures that if damage grows in regions of high damage level, at $q_\circ \cdot \vec{x} = 0, \pm 2\pi, \pm 4\pi, \dots$, the driving force would also grow in these regions, resulting in the unstable growth of damage. As $\tilde{\psi}(\vec{q_\circ}, d_\circ) \sim -\cos^4(\omega_\circ)$ where $\omega_\circ = \arctan(q_{y\circ}/q_{x\circ})$(see (18)), the interaction kernel in Fourier space $\tilde{\psi}$ is always negative and is exactly equal to zero for the polar angle $\omega_c = \pi/2$. As a result, the localization criterion reduces to

$$\mathcal{K}(d_\circ) = 0 \tag{43}$$

which coincides with the criterion for peak load. The inclination $\theta_{loc} = \pi/2 - \omega_c$ of the localization band is given by the most unstable mode (the one that first reaches the localization criterion described by (42)), namely the one that maximizes $\tilde{\psi}(\vec{q_\circ})$ and first satisfying the condition $\tilde{\psi}(\vec{q_\circ}) = 0$. The prediction of the emergence of an horizontal localization band ($\theta_{loc} = 0$), perpendicular to the main loading axis, is compatible with our experimental observations (Fig. 1C right panel and Video S1).

These results call for a few comments. First, under force control conditions, the localization threshold coincides with peak load. In other words, the heterogeneous mode of instability (i.e., the growth of the localization band within the specimen) is activated simultaneously with the homogeneous one (i.e., the unstable growth of the average damage level $d_\circ$). This is not the case under displacement control conditions as the extra term $-||\psi(d_\circ)||\Delta d_{\vec{x}}$ in the evolution equation (35) delays the homogeneous instability (that takes place after peak load) without affecting the threshold of the heterogeneous instability. The experimental observation of an increase of the precursory activity close to peak load for both loading conditions then supports that this phenomenon takes place at the approach of an instability, irrespective of its homogeneous or heterogeneous nature. In the following section, we detail the connection between the divergence of the precursor size and the presence of an instability at peak load.

Divergence of precursors

We study the variations of damage driving force on approaching peak load where damage localization occurs. Its linear expansion around the critical damage level d_c at peak load (and localization threshold) X_c follows

$$\mathcal{F}_\circ(d_\circ, X_\circ) = \mathcal{F}_\circ(d_c, X_c) + \frac{\partial \mathcal{F}_\circ}{\partial d_\circ}(d_\circ - d_c) + \frac{\partial \mathcal{F}_\circ}{\partial X_\circ}(X_\circ - X_c) + \frac{1}{2}\frac{\partial^2 \mathcal{F}_\circ}{\partial d_\circ^2}(d_\circ - d_c)^2 + \frac{1}{2}\frac{\partial^2 \mathcal{F}_\circ}{\partial X_\circ^2}(X_\circ - X_c)^2. \tag{44}$$

Equilibrium ensures that both $\mathcal{F}_\circ(d_\circ, X_\circ) = 0$ and $\mathcal{F}_\circ(d_c, X_c) = 0$. At peak load, we also have $\left.\frac{\partial \mathcal{F}_\circ}{\partial d_\circ}\right|_{X_c} = 0 \Rightarrow \mathcal{K}(d_c, X_c) = 0$. As a result, for $d_\circ < d_c$, (44) simplifies as

$$d_\circ = d_c - A_\circ \sqrt{X_c - X_\circ} \Rightarrow v_\mathrm{m} \propto 1/\sqrt{(X_c - X_\circ}. \tag{45}$$

where $A_\circ$ is a positive constant and $v_\mathrm{m} = \dot{d_\circ}$ is the average damage growth rate. Note that the second order term $\mathcal{O}(X_\circ - X_c)^2$ has been neglected. Reminding that $(X_c - X_\circ)$ is proportional to the distance to failure δ, we obtain $dE_\mathrm{d}/dt \propto \dot{d_\circ} \propto 1/\sqrt{\delta}$. Coming back to the evolution of the precursors, the dissipation rate dE_d/dt is given by the product of the precursor size with the precursor rate $dE_\mathrm{d}/dt = \langle S \rangle \, dN_\mathrm{S}/dt$. As we observe a constant activity rate, we thus expect the size S of precursors to diverge as

$$\langle S \rangle \propto 1/\sqrt{\delta}, \tag{46}$$

a prediction consistent with the experimental observations.

Numerical modeling of the evolution of the damage field

We solve the damage evolution equations (36) and (38) numerically to obtain accurate predictions of the exponents involved in the various scaling relations characterizing precursory cascades observed experimentally. An additional motivation of our numerical resolution of the damage evolution equations is to validate the assumptions that the statistical features of the specimen's intermittent response under force control conditions can be approximated from analyzing the damage cascades in an equivalent scenario constructed from displacement control experimental data. We consider an isotropic elasto-damageable specimen of size $L \times L$ discretized into L^2 elements with periodic boundary conditions. The degradation of the material elastic modulus with damage is described by a polynomial function $E_\circ = E^\circ(1 - d_\circ^2)$ with $E^\circ = 1$MPa, in line with the non-linear degradation of stiffness observed experimentally. This differs from the linear approximation made in most damage mechanics models [5]. Note however that similar non-linear descriptions have been adopted to describe the experiments [6**?**]. We remind that this continuum description of the damage induced softening through the damage dependent modulus $E_\circ(d_\circ)$ applies at a scale larger than the characteristic size of the microscopic dissipative mechanisms (e.g., microcracks) [7]. This continuous description also allows for modeling the non-local elastic interactions between material elements through the interaction kernel defined in (27), computed in (17) and represented in Fig.3*A* of the main article. To set the damage resistance, we use the experimentally measured hardening behavior $Y_{c\circ}(d_\circ) = Y_c^\circ(1 + \eta d_\circ)$ and consider $Y_c^\circ = 1.4$ kJ/m^3 and $\eta = 40$. The field of Y_c has an initial Gaussian disorder $N(0, 0.05)$ accounting for y_c in the theoretical formulation. The value of incremental damage $\delta d_\circ$ to be added whenever the damage criterion is fulfilled is taken as 0.001. Using the above parameters, we simulate twenty realizations each for force and displacement imposed conditions and analyze the intermittent damage evolution preceding localization.

Force control case

We adopt the numerical procedure employed by Berthier et al. [8] to simulate damage evolution (36) under quasi-static loading conditions. We increase the stress gradually to ensure that damage grows by an increment $\delta d_\circ$ in one material element at the location $\vec{x} = \vec{x}_0$ so that $d(\vec{x}_0) \to d(\vec{x}_0) + \delta d_\circ$. Hence, there is no explicit time defined in the simulations. The value of $Y(x_0)$ at the location $\vec{x}_0$ is increased by an increment $Y' \delta d_\circ$ and $Y_c(\vec{x}_0)$ is increased by an increment $(Y_c' \delta d_\circ + y_c(x_0))$ where $y_c(x_0) \ll Y_c' \delta d_\circ$. As $Y' < Y_c'$, owing to the stability of the damage growth process, no additional damage event takes place at $\vec{x}_0$. However, the non-local redistribution of damage driving force, given by

$\delta d_\circ \psi(\sigma_0)(\vec{x}-\vec{x}_0)$, may trigger another damage event elsewhere and ultimately a damage cascade. Once the cascade is over, the stress is increased again. The initial disorder in the damage resistance ensures that cascades are small at the early stages of the damage process, i.e., redistributions do not trigger large cascades. On approaching failure, the damage cascades' size increases and their corresponding spatial extent reaches the system size at localization. As the redistributions span the entire system, multiple clusters may nucleate during a cascade. The intermittent damage evolution is thus formulated as arising from the co-action of the disorder and long-range interactions.

Precursors to damage localization

The computed stress-strain response during damage evolution is presented in Fig. 4*A* and consists of a sequence of force plateaus followed by elastic loading (inset of Fig. 4*A*). The evolution of damage at various distances to failure for a typical numerical experiment is presented in Fig. 4*B* manifesting a homogeneous damage evolution until localization. The localization band depicted in the final panel is in good agreement with the theoretical predictions $\theta_{loc}=0$. Each cycle of redistribution, irrespective of the number of elements being damaged, is assumed to constitute a single damage event of energy A as incremental damage in elements are assumed to occur simultaneously. The energy of the cascade is therefore $S=\sum A$. Further, the number of redistribution cycles is taken as the duration of the cascade (T) and the spatial extent of the largest cluster is taken as the characteristic length of the cascades (ξ). The cascades' energy and duration are shown to scale with the characteristic length ξ with exponents $d_{\rm f}\simeq 1.15$ and $z\simeq 0.62$, see Figs. 4*C* and 4*D*. The sizes of the cascades are distributed as a power law, Fig. 4*E*, with $\beta\simeq 1.36$. Considering all cascades from the beginning of the compression experiment, we measure a larger exponent $\beta_{\rm tot}\simeq 2.2$. The relation between both exponents is derived by taking into account the non-stationary nature of damage evolution. The relation $\beta<\beta_{\rm tot}$ results from the divergence of the exponential cut-off S^* to the distribution of avalanche sizes [9]

$$P_\delta(S)=C_o S^{-\beta}\exp\left(\frac{-S}{S^*}\right). \tag{47}$$

where C_o is a normalization constant and $S^*\sim\delta^{-\alpha(2-\beta)}$. The last relation is inferred from the divergence $\langle S\rangle\sim\delta^{-\alpha}$ of the average cascade size $\langle S\rangle$ and its relation with S^* through

$$\langle S\rangle=\int_0^\infty S P_\delta(S)dS\rightarrow\langle S\rangle\sim S^{*(2-\beta)}. \tag{48}$$

The sizes' distribution of all the cascades of an experiment, until failure i.e., for $\delta\in[0,1]$ is

$$P(S)=\frac{C_o}{N_{\rm tot}}\int_0^1\frac{dN_S}{dt}(\delta)P_\delta(S)d\delta, \tag{49}$$

where $\frac{dN_S}{dt}(\delta)$ is the rate of cascades at some distance to failure δ and is a constant. Using the relation between $\langle S\rangle$ and S^* and the scaling of $\langle S\rangle$ with δ, we have

$$P(S)=\frac{C_o}{N_{\rm tot}}\int_0^1\delta^{-\epsilon}S^{-\beta}\exp\left(S\delta^{\frac{\alpha}{(2-\beta)}}\right)d\delta. \tag{50}$$

$$\Rightarrow P(S)\sim S^{-\beta_{\rm tot}}\sim S^{-\beta-(\epsilon+1)(2-\beta)/(\alpha)}\rightarrow\beta_{\rm tot}=\beta+\frac{2-\beta}{\alpha} \tag{51}$$

This relation is consistent with the exponents measured in our simulations.

Variation of the size and the activity rate of damage cascades on approaching damage localization

The variation of average cascade size $\langle S\rangle$ with the distance to failure is shown in Fig. 4*F*. We measure the exponent $\alpha\simeq 0.48$. The activity rate of cascades, dN_S/dt, is found independent of the distance to failure (Fig. 4*G*) similar to our experimental observations.

Implications of a non-positive interaction kernel

The non-positive nature of the elastic interactions provide interesting additional traits to the critical features of the damage field. In particular, as only a fraction of material elements are loaded while the others are shielded after each damage event, the (marginal) stability of the elements is altered after each redistribution cycle. Here, we explore the stability numerically by introducing the distance to local failure $\delta Y(\vec{x}) = Y_c(\vec{x}) - Y(\vec{x})$. An additional non-trivial exponent $\theta > 0$ has been shown to characterize the distribution $P(\delta Y)$ of the distance to local failure in case of yielding of amorphous materials [10–12]. A similar description also holds for elasto-damage solids. The exponent characterizing $P(\delta Y)$ is measured in Fig. 4*H*. The exponent θ takes a small value $\simeq 0.14$ and, unlike other critical exponents β, d_f and z, increases on approaching failure [11, 12] to a value $\theta \simeq 0.35$. This increase might be due to the increasing amplitude of the pre-factor of the interaction kernel $||\psi||$. Another interesting manifestation of the non-positive elastic interactions is the constant depth of the cascades, i.e, the interface never progresses locally by more than one elementary step $\delta d_\circ$ during a cascade. The variation of the characteristic depth Δd^* with the distance to failure is found to be constant in Fig. 4*I*, implying that all material elements damage once during a cascade.

We also validate numerically our method of deducing the nature of elastic interactions from the incremental damage field during a cascade that we used experimentally to characterize the elastic interactions. Figure 4*J* shows the variations along the X-axis of the 2D auto-correlation function $C(\vec{\delta r}) = \langle \delta d(\vec{r}) \cdot \delta d(\vec{r} + \vec{\delta r}) \rangle_{\vec{r}}$ of the incremental damage field averaged over several avalanches. The correlations are found to decay as $\sim 1/\delta r^2$. Overall, we obtained a detailed statistical description of precursory activity for the force control scenario from our numerical model. In addition, it captures quantitatively the main features observed experimentally. In the next section, we explore numerically the damage field evolution under displacement control conditions and validate the protocol employed experimentally for studying avalanches under equivalent force control conditions.

Equivalent force control case

We now simulate damage spreading under displacement control conditions. We follow the same numerical scheme as mentioned previously for the force control case. In addition, we include the term $-||\psi||\langle \Delta d \rangle_{\vec{x}}$ to the local driving force Y, in line with the damage evolution equation (38). Consequently, under these loading conditions the damage growth manifests as load drops at fixed displacement.

Using the methodology proposed in the main manuscript for the analysis of experimental data, we obtain an equivalent force control scenario from the displacement control simulations (inset of Fig. 5*A*). A comparison of the spatial structure of damage cascades in the equivalent scenario with cascades during force control condition are presented in Fig. 5*B*. They show remarkable differences while their statistics are similar as we will see in the following. Notably, cascades in the equivalent force control conditions appear as two dimensional, in qualitative agreement with the experimental observations, see inset of Fig. 2*A*. We then determine the exponent z/d_{f} describing the scaling relation between cascade size S and its duration $T \simeq 0.64$, see Fig. 5*C*. The distribution of the cascade sizes is characterized by power-law relations with exponents $\beta \simeq 1.35$ and $\beta_{\mathrm{tot}} \simeq 2.2$ as shown in Fig. 5*D*. Similar to the force control case, the exponents characterizing the distribution of distance to local failure is non-zero. Interestingly, the value $\theta \simeq 0.18$ observed for the present case is much smaller than the force control case as shown in Fig. 5*E*. This is perhaps due to the presence of the stabilizing term $\sim -\langle \Delta d \rangle_{\vec{x}}$ in displacement loading condition that impedes the spatial organization of cascades. Nevertheless and most importantly, the divergence of the average cascade size and the constant activity rate on approaching failure are similar to the features observed under force control, as shown in Fig. 5*F* and Fig. 5*G*, respectively. This highlights the universal nature of the intermittent material response approaching bifurcation at peak load. The divergence of the rate of dissipation is therefore $dE_d/dt \propto 1/\sqrt{\delta}$. In terms of load drops, the event activity rate is shown to vary with distance to failure in Fig. 5*H*. Lastly, we observe that the radial decay of the 2D correlation function of incremental damage field taken along the X-axis as well as the depth of cascades during the displacement control simulations resemble the results obtained under force control, see Fig. 5*I* and Fig. 5*J*. Thus, we show here that using an equivalent force control scenario results in cascades that are statistically similar to that obtained under force control conditions. The differences in exponents are rather minimal except in case of θ which characterizes the local stability of damage field between precursors instead of the nature of precursors themselves. Also, the activity rate of cascades in both scenarios were a constant. Such considerations thus allow for an improved understanding of the spatio-temporal structure of damage cascades in our experiments which otherwise in true force controlled conditions would be challenging for observation.

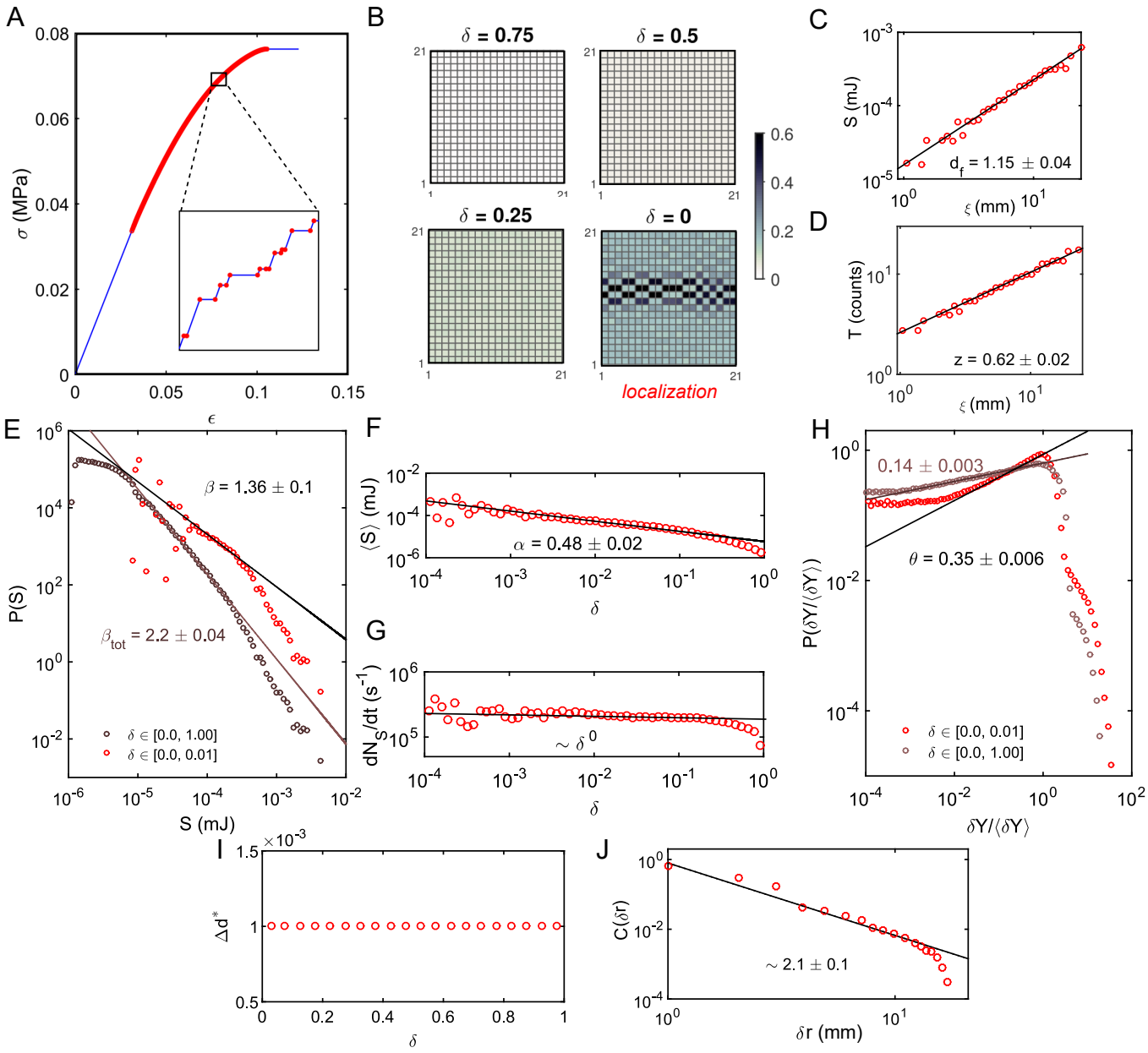

FIG. 4. (A) Typical stress-strain response obtained during the simulations of damage spreading under force control conditions show jumps of displacement at constant force corresponding to damage growth. Damage localization takes place at peak load. After it, damage evolution becomes unstable. (B) Snapshot of the damage field at various distances from failure. Damage grows rather homogeneously until localization. Variation of (C) cascade size S and (D) duration, T with the spatial extent ξ are related by robust scaling exponents, thus defining the fractal dimension d_f and dynamic exponent z. (E) The distribution of cascade sizes S computed at different ranges of δ on approaching failure reveals the non-stationary nature of damage evolution, i.e., two different scaling exponents. The average size of cascades is shown to diverge as a power-law on approaching failure (F) Their activity rate remains constant, (G). (H) Distribution of distance to local failure, δY defining the exponent $\theta > 0$ reminiscent of the non-positive interaction kernel. (I) Variation of the characteristic damage increment of an avalanche with distance to failure δ. (J) Spatial correlation of incremental damage field along X-axis displaying a decay $\sim 1/r^2$ reminiscent of the interaction kernel $\psi \sim 1/r^2$.

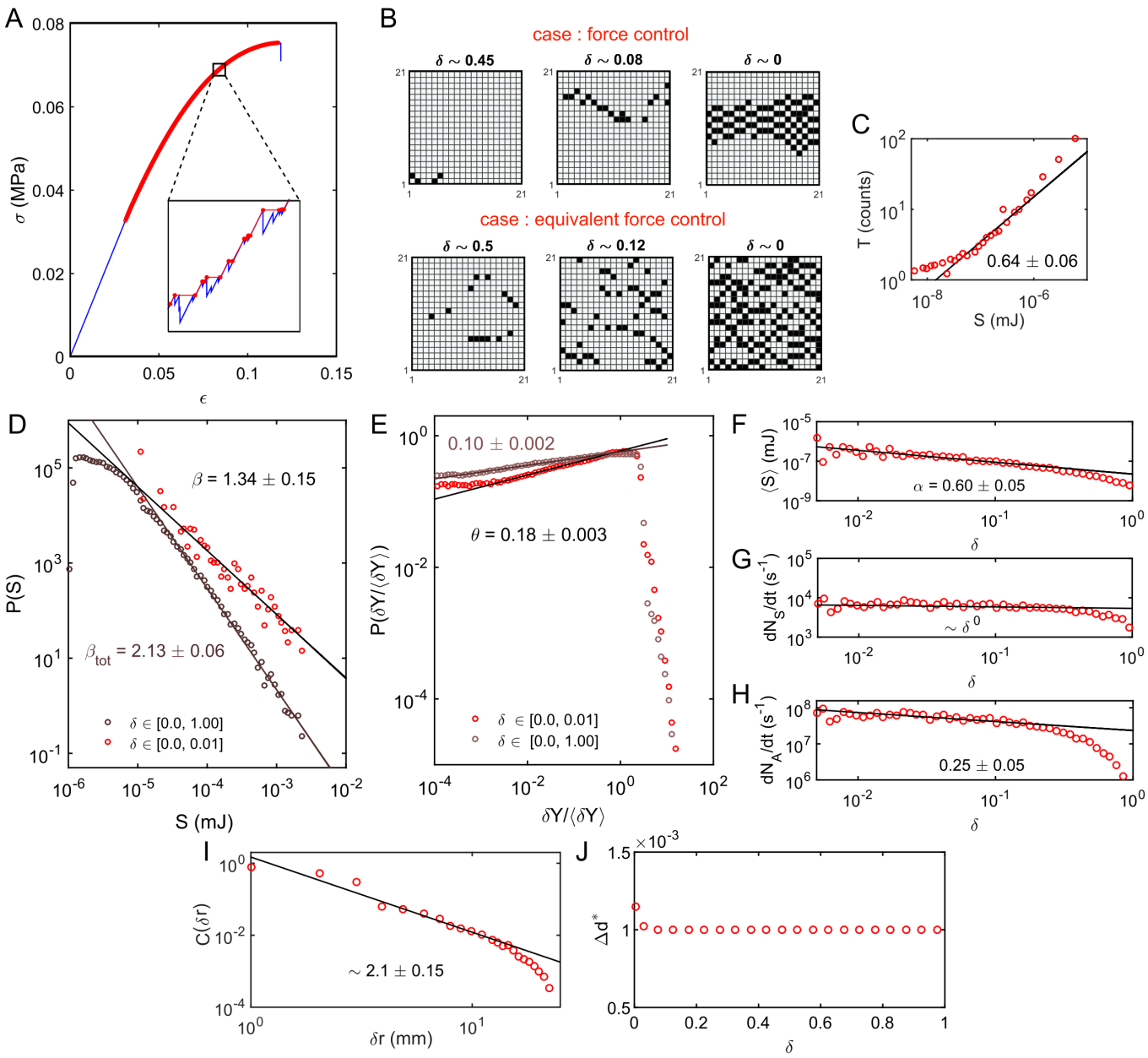

FIG. 5. (A) Typical stress-strain response obtained during the simulations of damage spreading in displacement control conditions show load drops at constant displacement corresponding to damage growth. We construct an equivalent force control scenario from load drops similar to the experiments to obtain damage cascades. (B) Snapshot of the incremental damage field during a damage cascade at various distances from failure in force control condition is compared to the equivalent scenario. Note the cascades in equivalent force control case has more clusters and is spatially distributed. (C) Scaling of duration T with cascade size, S. (D) Size distribution of cascade size at different ranges of δ. (E) Size distribution of distance to local failure, δY, in the vicinity of failure, $\delta \in [0, 0.01]$ and $\delta \in [0.25, 0.5]$. Variation of (F) average cascade size, (G) activity rate of cascades and (H) event activity rate (load drops) with distance to failure, δ. (I) Variation of 2D correlation of incremental damage field along X-axis with distance. (J) Variation of the characteristic damage with distance to failure δ.

Comparison of exponents with literature and prediction for 3D disordered solids

As few models incorporating long-range interactions exist for compressive failure [6], we compare in Table II the exponents measured in our work with predictions from elasto-plastic models of yielding of amorphous solids as they also feature a non-positive long-range redistribution kernel. In these studies [10, 13, 14], the kernel is of the shear-type:

TABLE II. Comparison of exponents with numerical and experimental data from literature.

		present work		literature : numerical		
	expression	experiment	numerical	case - 2D	case - 3D	literature (exp.)
d_{f}	$S \propto \xi^{d_{\mathrm{f}}}$	1.07 ± 0.07	1.15	1.15^a, 1.10^b, 0.90^c	1.50^b, 1.38^c	2.0^e, 2.1^f
z	$T \propto \xi^z$	0.53 ± 0.11	0.62	0.57^b, 0.57^c	0.65^b, 0.82^c	1.0^e
θ	$P(\delta Y) \propto \delta Y^\theta$	0.24 ± 0.03	0.35 (0.18)	0.57^b, 0.52^c,	0.35^b, 0.37^c, 0.2^d	-
β	$P(S) \propto S^{-\beta}$	1.30 ± 0.11	1.36 (1.34)	1.8^a, 1.35^b, 1.28^c	1.45^b, 1.25^c, 1.2^d	1.4^e, 2.1^f
α	$S \propto \delta^{-\alpha}$	0.57 ± 0.04	0.48 (0.60)	0.4^a	-	1.3^e, 2.6^f
z/d_{f}	$T \propto S^{z/d_{\mathrm{f}}}$	0.49 ± 0.14	0.53 (0.64)	0.51^b, 0.63^c	0.43^b, 0.58^c	0.5^e
β_{tot}	$\beta_{\mathrm{tot}} = \beta + \frac{2-\beta}{\alpha}$	2.32 ± 0.18	2.2 (2.13)	2.7^a, 2.65^b, 2.72^c	2.55^b, 2.62^c, 2.8^d	1.75^e, 2.5^f

The values in brackets in fourth column are obtained for the case of equivalent force control from displacement control simulations. Exponents of [a]Girard *et al.* [6] and [d]Ozawa *et al.* [14] are for cascades preceding the critical stress while exponents in [b]Lin *et al.*[10] and [c]Liu *et al.* [13] were obtained for stationary cases of yielding in amorphous materials. [e]Vu *et al.* [15] examine the failure of concrete samples using acoustic emission and [f]Kandula *et al.* [16] process the X-ray tomography image stack of Carrara marble specimens.

the driving force is reloaded for the elements along the diagonals and unloaded for those along the horizontal and vertical axes. Our observations are shown to be in good agreement with the theoretical predictions for the 2D case, except for the exponent θ. The difference arises from the different kernels considered theoretically that corresponds to shear and the one involved in our experiments that corresponds to compression. This also explains why the exponents observed in our experiments match well with predictions drawn from our simulations, which consider a compression kernel. We believe that the exponents predicted for the 3D case constitute realistic predictions for precursory cascades during compressive failure of disordered materials. These predicted values might be significantly different from the exponents measured experimentally [15, 16]. We believe that the procedure employed to analyze their experiments does not capture the full damage cascades, but instead the individual clusters composing it. Note also that the limited spatial resolution (studies using acoustic emission [15]) or temporal resolution (studies based on X-ray tomography [16]) might hinder the complete characterization of damage cascades from individual damage events in these studies.

Movies

The two movies available online describe the spatio-temporal structure of the damage cascades measured during compressive failure. The first movie provides the global and local damage evolution as well as the raw images as obtained from the camera. The second video highlights the highly correlated clusters constituting a damage cascade as given in Fig.2*B* of the main article.

- **Video-1.mp4** : (A) Typical force-displacement response during compression experiments. A red tracer marks the damage cascades on the curve. (B) Images of the deformation of the cells recorded by our high speed camera. Note that the localization band is barely visible to the naked eye at peak load but becomes prominent afterwards as progressive collapse of the cells in the band takes place. (C) The coordinates of the cells from the particle tracking (marked as +) superposed over the map of dissipation energy density for various damage cascades. (D) Variations of cascade sizes S with distance to failure δ, updated with each new cascade whose size is displayed at the top right corner

- **Video-2.mp4** : (A) Spatial structure of the damage clusters as deciphered from a single time step. (B) The augmented spatio-temporal organization of the various clusters constituting the damage cascade shown in middle panel of Fig. 2*A*

* Current address : Arnold-Sommerfeld-Center for Theoretical Physics and Center for NanoScience, Ludwig-Maximilians-Universität München, D-80333 München, Germany
† laurent.ponson@upmc.fr

[1] J. Schindelin, I. Arganda-Carreras, E. Frise, V. Kaynig, M. Longair, T. Pietzsch, S. Preibisch, C. Rueden, S. Saalfeld, B. Schmid, *et al.*, Fiji: an open-source platform for biological-image analysis, Nature Methods **9**, 676 (2012).
[2] B. Glasser and I. Goldhirsch, Scale dependence, correlations, and fluctuations of stresses in rapid granular flows, Physics of Fluids **13**, 407 (2001).
[3] E. Berthier, V. Démery, and L. Ponson, Damage spreading in quasi-brittle disordered solids: I. localization and failure, Journal of the Mechanics and Physics of Solids **102**, 101 (2017).
[4] V. Dansereau, V. Démery, E. Berthier, J. Weiss, and L. Ponson, Collective damage growth controls fault orientation in quasibrittle compressive failure, Physical Review Letters **122**, 085501 (2019).
[5] J. Lemaitre, *A course on damage mechanics*, Amsterdam (Springer Verlag, 1992).
[6] L. Girard, D. Amitrano, and J. Weiss, Failure as a critical phenomenon in a progressive damage model, J. Stat. Mech. **.**, P01013 (2010).
[7] M. Kachanov, Elastic solids with many cracks and related problems, Advances in Applied Mechanics **30**, 259 (1993).
[8] E. Berthier, A. Mayya, and L. Ponson, Damage spreading in quasi-brittle disordered solids: Ii. what the statistics of precursors teach us about compressive failure, Journal of the Mechanics and Physics of Solids **162**, 104826 (2022).
[9] D. Amitrano, Variability in the power-law distributions of rupture events, Eur. Phys. J.: Spec. Top. **205**, 199 (2012).
[10] J. Lin, E. Lerner, A. Rosso, and M. Wyart, Scaling description of the yielding transition in soft amorphous solids at zero temperature, Proceedings of the National Academy of Sciences **111**, 14382 (2014).
[11] J. Lin, T. Gueudré, A. Rosso, and M. Wyart, Criticality in the approach to failure in amorphous solids, Physical Review Letters **115**, 168001 (2015).
[12] J. Lin and M. Wyart, Mean-field description of plastic flow in amorphous solids, Physical Review X **6**, 011005 (2016).
[13] C. Liu, E. E. Ferrero, F. Puosi, J.-L. Barrat, and K. Martens, Driving rate dependence of avalanche statistics and shapes at the yielding transition, Physical Review Letters **116**, 065501 (2016).
[14] M. Ozawa, L. Berthier, G. Biroli, A. Rosso, and G. Tarjus, Random critical point separates brittle and ductile yielding transitions in amorphous materials, Proceedings of the National Academy of Sciences **115**, 6656 (2018).
[15] C. C. Vu, D. Amitrano, O. Plé, and J. Weiss, Compressive failure as a critical transition: Experimental evidence and mapping onto the universality class of depinning, Phys. Rev. Lett. **122**, 015502 (2019).
[16] N. Kandula, B. Cordonnier, E. Boller, J. Weiss, D. K. Dysthe, and F. Renard, Dynamics of microscale precursors during brittle compressive failure in carrara marble, J. Geophys. Res. Solid Earth **124**, 6121 (2019).